THE UNIVERSITY OF CHICAGO

MULTI-MESSENGER ASTRONOMY WITH ADVANCED LIGO-VIRGO

A DISSERTATION SUBMITTED TO
THE FACULTY OF THE DIVISION OF THE PHYSICAL SCIENCES
IN CANDIDACY FOR THE DEGREE OF
DOCTOR OF PHILOSOPHY

DEPARTMENT OF ASTRONOMY AND ASTROPHYSICS

BY

HSIN-YU CHEN

CHICAGO, ILLINOIS

DECEMBER 2017

TABLE OF CONTENTS

LIST OF FIGURES

LIST OF TABLES

ACKNOWLEDGMENTS

It was a long and spectacular journey. It is difficult to describe how many thanks I have to my thesis advisor Daniel Holz. He took me as a student when my academic path was hazy. He has a broad and creative science vision, and has always been very hand-on and patient at work. As an advisor, he gave me full support and protection. As someone I worked close to, he has been very understanding and accommodating, nevertheless it was his endless momentum and enthusiasm in science that pushed me over these years.

I was extremely lucky to have my thesis realized by two remarkable collaborations: LIGO and DECam. I learned how to work in a big collaboration with my LIGO colleagues: Marica Branchesi, Leo Singer, Reed Essick, Erik Katsavounidis, Matthew Evans, Benjamin Farr, Jolien Creighton, Jocelyn Read, Ian Harry and many others. The Dark Energy Survey-Gravitational Wave group is a smaller but very warm collaboration because of Marcelle Soares-Santos and James Annis. It was because of their persistency on the big dream that inspired me and led to the success of this collaboration.

Thank you to my thesis committee members: Scott Dodelson, Craig Hogan, and Stephan Meyer.

I want to thank my friends and office mates in Chicago over the years: Laura M Mocanu, Ke Fang, Sean Johnson, Vinicius Miranda, Zoheyr Doctor, Maya Fishbach, Yuan Lin, Yu-Ching Shih, Yung-Tsen Chen, Chih-Chieh Hsu, Victor Lee, Shang-Huei Liang, and Grace Lee. Special thank to Tsung-Han Chou, who offered me full support, tolerance and company over years. He brought happiness and made lots of difficult days easier. Another special thank to Ting-Chun Kuo and Shih-Wen Chen for always being there when I need. I would not be able to go through these years without them. Thank you to Salvatore Vitale who has an unbeatable sense of humor and broaden my views in many aspects. Thank you to Liwen Chen for first being my literature teacher and then an all time shelter and tutor who provided me subjective observations, advice, and relief.

Finally, I would like to acknowledge my family. Thank you to my Mom and Dad who offered me complete support and trust to my various major choices in life, even for some they did not feel like they completely understood them. Thank you to my brother for paving the way in physics, and always being a good companion and advisor in my academic path.

ABSTRACT

The first direct detections of gravitational waves by the Laser Interferometer Gravitational-wave Observatory initiated the era of gravitational wave astronomy (Abbott et al., 2016; Abbott et al., 2016b, 2017a). Gravitational waves serve as a new and independent probe of the Universe. The combination of gravitational waves with information from other messengers, such as electromagnetic emission from binary neutron star inspiral (Abbott et al., 2017b), will lead to a more complete and accurate understanding of cosmology and astrophysics.

My thesis is focused on gravitational wave multi-messenger astronomy. The most promising sources for current gravitational wave detectors are compact binary mergers, including the mergers of stellar mass binary black holes, binary neutron stars, and neutron star-black hole system. I investigated the detection rate of binary neutron star and neutron star-black hole mergers from observations of their potential electromagnetic emission. To facilitate the search for the electromagnetic counterparts and the host galaxies of compact binaries, I developed a rapid algorithm that reconstructs the sky direction and luminosity distance of binary mergers from their gravitational wave signals, and predicted the existence of well-localized events. In addition, I carried out a thorough study of how gravitational-wave observational selection effects influence electromagnetic follow-up.

In summary, I explored how to measure astrophysical and cosmological parameters with gravitational wave detections, and facilitated gravitational wave-electromagnetic follow-up through various approaches, paving the way for the future of gravitational wave astrophysics and cosmology.

CHAPTER 1

INTRODUCTION

In 1915, Albert Einstein published the theory of general relativity (Einstein, 1916), marking a milestone in modern physics. One prediction from general relativity is the existence of gravitational waves (GWs) (Einstein, 1918). Non-spherical and rotationally asymmetric accelerating masses distort the space-time and generate GWs. However, for a long time, the amplitude of GWs was significantly lower than human achievable sensitivity. In 1975, Hulse and Taylor discovered the binary pulsar PSR B1913+16 (Hulse & Taylor, 1975), and later Taylor and Weisberg demonstrated that the energy lost by the binary can be well explained by emission in the form of GWs (Taylor & Weisberg, 1982). This was the first indirect detection of GWs. It was not until 2015 that the Laser Interferometer Gravitational-wave Observatory (LIGO) (Abbott et al., 2016) directly captured GW signals arriving on earth from a binary black hole merger for the very first time thus initiating the era of GW physics and astronomy.

Compact binary coalescences (CBCs) are ideal GW sources. Binary systems can generate quadruple radiation, and the strain of the GWs from a binary goes as

$$h \sim 2\frac{G^2}{c^4}\frac{m_1 m_2}{D_{\rm L} r} \tag{1.1}$$

where G is the gravitational constant, c is the speed of light in vacuum, m_1 and m_2 are the two masses in the binary, r is the orbital seperation, and $D_{\rm L}$ is the luminosity distance from the binary system to the observer. Compact stars such as neutron stars (NSs) and black holes (BHs) are able to get close (a few Schwarzschild radii) without merging. A 30-30 $M_\odot$ binary BH system at its last stable orbit (6 Schwarzschild radii) located 1 Gpc away leads

to $h \sim 10^{-21}$. The frequency of GWs is twice the binary orbital frequency:

$$f_{\rm GW} = 2f_{\rm orbit} = \frac{1}{\pi}\sqrt{\frac{G(m_1+m_2)}{r^3}} \tag{1.2}$$

For the same binary at the last stable orbit, this corresponds to $f_{\rm GW} \sim 25$ Hz. These strain and frequency ranges are optimal for a kilometer-scale ground-based Michelson interferometer GW observatory. Therefore stellar mass CBCs in the local Universe are primary targets of current generation ground-based GW detectors (Abbott et al., 2016a).

Observing GWs from stellar mass CBCs brings about opportunities to study various problems in physics and astronomy. We started to learn about the formation channel of these systems (Abbott et al., 2016a,c). Furthermore, the detection of GWs from such mergers allows for testing general relativity in the strong field limit (Abbott et al., 2016b; Yunes et al., 2016). Nevertheless, electromagnetic (EM) observations have helped to establish our understanding of GW sources, and will continue to supplement GW observations for the best possible scientific outcome. For example, determining the Hubble constant by combining the luminosity distance measured from GWs and the redshift measured from EMs for a given source will potentially provide a different insight into the tension between different measurements of the Hubble constant (Schutz, 1986; Dalal et al., 2006; Nissanke et al., 2013a; Del Pozzo, 2014). A joint observation of a short gamma-ray burst (GRB) and CBC will answer the long standing mystery regarding the progenitor of short GRBs (Berger, 2011, 2014). There are also searches for 'kilonovae' associated with binary NSs that might account for the excess of heavy elements in the Universe (Barnes & Kasen, 2013; Tanvir et al., 2013; Berger et al., 2013). Among these interesting problems, my thesis is focused on facilitating the following aspects of GW-EM multi-messenger astronomy:

- The rate of binary NS (BNS) and NSBH mergers are highly uncertain. I investigated the detection rate of BNS and NSBH mergers in relation to their potential EM counterparts, short GRBs. Reversely, comparing the coalescence rate estimated from GWs to

the short GRB rate will constrain the formation channels of CBCs and the properties of short GRBs. (Chapter 2)

- To jointly observe GW and EM signals from a source, sharing the location of the source in a timely manner is the primary requirement. I have developed a rapid algorithm that localizes the sky direction and luminosity distance of CBCs. With this algorithm, I conducted an end-to-end study of how well the ground-based GW detector network will localize CBCs in the next few years. (Chapters 4 and 5)

- Locating he host galaxy of the CBC is another method to measure the redshift and to study the environment of CBCs. My thesis pointed out that well-localized GW events can appear in the next few years, allowing for host galaxy identification. The utility of this small sample of events may outweigh the rest of the population. (Chapters 3 and 5)

- I have helped the Dark Energy Survey-Gravitational Wave working group to optimize the use of the Dark Energy Camera's telescope time for the follow-up of the first GW detections (Soares-Santos et al., 2016; Annis et al., 2016; Cowperthwaite et al., 2016). Combining my experiences in GW astronomy and EM follow-up, I carried out a thorough study of the influence of GW selection effects on EM follow-up. (Chapter 6)

In summary, my research has laid the foundation for the GW detection era, and has been applied in various directions to realize GW science.

CHAPTER 2

GAMMA-RAY-BURST BEAMING AND GRAVITATIONAL-WAVE OBSERVATIONS

2.1 Introduction

There has been an active program of observing gamma-ray bursts (GRBs), focusing on rapid follow-up to determine afterglows and identify host galaxies (Soderberg et al., 2006; Panaitescu, 2006; Berger et al., 2007; Perley et al., 2009). There is growing evidence that most, if not all, short/hard gamma-ray bursts are associated with the mergers of either two neutron stars, or a neutron star with a black hole (Fong et al., 2010; Church et al., 2011; Berger, 2011). These studies have also provided redshifts for a subsample of short GRBs, thereby providing preliminary estimates for the rate densities of these events (Nakar et al., 2006; Dietz, 2011). There is tremendous interest in combined gravitational wave and electromagnetic multi-messenger observations of these GRBs (Metzger & Berger, 2012; Evans et al., 2012; Abadie et al., 2012b), as this would help confirm the first detections of gravitational-waves (GWs) from mergers involving a neutron star, elucidate the properties of GRBs, and potentially provide interesting measurements of the Hubble constant and the dark energy equation-of-state (Schutz, 1986; Holz & Hughes, 2005; Dalal et al., 2006; Nissanke et al., 2010).

One of the most important properties of GRBs is the beaming of the gamma rays during the burst, which relates the observed and total energies of the explosions, and is a crucial factor in estimating the intrinsic GRB event rate. Recent observations suggest beaming opening angles of 1–30° (Soderberg et al., 2006; Burrows et al., 2006; Fong et al., 2012; Coward et al., 2012), with numerical studies finding consistent values (Popham et al., 1999; Rosswog & Ramirez-Ruiz, 2002; Janka et al., 2006; Rezzolla et al., 2011).

In this chapter we estimate the limits that arise on the beaming of short-duration GRBs

based on the non-detection of GWs from associated binary systems in existing LIGO/Virgo data. We also make projections for the detection rate of binary systems, as a function of mass and beaming angle, for future networks of GW observatories. We emphasize that this rate is *observationally* determined, although it is broadly consistent with the rates arising from population synthesis (Belczynski et al., 2006; O'Shaughnessy et al., 2008; Belczynski et al., 2010; Abadie et al., 2010a; Dominik et al., 2012). We also compare the GW detection rates of untriggered and triggered short GRBs.

In what follows we assume that all short GRBs are associated with low-mass compact binary coalescences. While it is conceivable that not all short GRBs are the result of binary coalescences, it is perhaps even more likely that not all binary coalescences result in GRBs. We thus expect that our predictions for the event rates are conservative.

2.2 LIGO S6/Virgo VSR2

From July 2009 to October 2010 the LIGO (Hanford [H] and Livingston [L]) and Virgo [V] observatories conducted a search (S6/VSR2–3) for compact binary coalescences. They did not detect any gravitational-wave events, and thereby established upper limits on the event rates of coalescences in the local Universe (Abadie et al., 2012c).

We follow the approach of Dalal et al. (2006), taking the representative sensitivities presented in Fig. 1 of Abadie et al. (2012c), and calculating the corresponding horizon distances. As was done in the LIGO compact binary coalescence searches (Abadie et al., 2012), we ignore data below a frequency cut-off of $f_{\rm low} = 40\,{\rm Hz}$ for the LIGO detectors, and $f_{\rm low} = 50\,{\rm Hz}$ for Virgo, with upper limits set by the frequency of the innermost stable circular orbit. We use non-spinning waveforms based on the stationary phase approximation (Dalal et al., 2006); comparable results would be found with the inclusion of spin (Nitz et al., 2013). We utilize the approach of Schutz (2011) to combine the antenna patterns of different interferometers, taking into account the differing horizon distances (which are functions of

the masses) as well as power patterns.

Since the LIGO/Virgo network has not detected a gravitational wave source, it provides a 90% upper limit to the rate density: $\mathcal{R} = 2.3/(\sum_i \bar{V}_i \times \Delta t_i)$, where the sum is over the different detector networks configurations, $\bar{V}_i$ is the mean detectable volume, Δt_i is the amount of observational time, and the factor of 2.3 is in accordance with a Poisson process (see the discussion below Eq. 2.1). Although to date the LIGO/Virgo collaboration has performed coincident searches (wherein individual observatories separately and independently detect a source), in the future they are expected to utilize coherent network analysis (wherein data from multiple observatories is combined and analyzed as an ensemble, increasing the overall sensitivity of the network). We follow a coherent approach, and calculate the coherent network signal-to-noise (SNR) threshold, ρ, which we would need to apply, as a function of mass, to match the rate limits which come out of the full analysis presented in Abadie et al. (2012c), finding a range $\rho = 10.7$–12.2, with the specific value depending on the mass and mass ratio of the binaries. In the next section we utilize this same SNR threshold to make predictions for future advanced networks. Abadie et al. (2012c) assume a uniform distribution of component masses for their binaries. We also consider the case where the neutron star is restricted to have $m_1 = 1.4\,M_\odot$, and the mass of the companion is given by $m_2 = M_{\rm total} - m_1$. Because this entails higher mass ratios for higher mass binaries, it decreases the overall gravitational-wave strength of the sources in comparison to the uniform distributions, and therefore decreases the detectable volume. At $M_{\rm total} \sim 3\,M_\odot$ we find a rate limit of NS-BH binaries of $4.5 \times 10^{-4}{\rm Mpc}^{-3}{\rm yr}^{-1}$, comparable to the uniform rate in Abadie et al. (2012c), with the rate rising to $6.1 \times 10^{-5}{\rm Mpc}^{-3}{\rm yr}^{-1}$ at $M_{\rm total} = 15\,M_\odot$ and $6.6 \times 10^{-5}{\rm Mpc}^{-3}{\rm yr}^{-1}$ at $M_{\rm total} = 25\,M_\odot$.

We are interested in relating the observed event rates to the beaming angles of GRBs. We define the beaming angle, θ_j, to be the half opening angle of one of the two polar jets of a gamma-ray burst. Given the paucity of data on the beaming of short GRBs, it is premature to

assume knowledge of the distribution of beaming angles. We therefore assume that all short GRBs have a fixed beaming angle, θ_j, defined by $1/(1-\cos\theta_j) \equiv \int P(\theta)/(1-\cos\theta)\, d\theta$, where $P(\theta)$ is the true distribution of beaming angles. The implied rate density of these coalescences is given by $\mathcal{R} = \mathcal{R}_{\rm GRB}/(1-\cos\theta_j)$. In what follows we assume a conservative observed rate of short GRBs of $\mathcal{R}_{\rm GRB} = 10\,{\rm yr}^{-1}{\rm Gpc}^{-3}$, based primarily on BATSE and *Swift* observations (Nakar et al., 2006; Dietz, 2011; Coward et al., 2012); the GW detection rate scales linearly with this intrinsic rate. Given the lack of detected binaries in the existing LIGO/Virgo data, we find that the minimum value of the beaming angle ranges from $\theta_j > 0.8^\circ$ for binaries with $M_{\rm total} = 3\,M_\odot$, rising to 3.5° for $15\,M_\odot$ and 4.5° for $25\,M_\odot$, assuming a uniform distribution of mass ratios and including the prior from the S5 results (Abadie et al., 2010b). If we require one member of the binary to have $M_1 = 1.4\,M_\odot$, these numbers become $0.3^\circ/1.0^\circ/0.9^\circ$ for $M_{\rm total} = 3/15/25\,M_\odot$, without the S5 prior. These limits are completely consistent with observations and expectations. However, given that GRBs have recently been observed with $\theta_j \sim 5^\circ$, it is apparent that even the current LIGO/Virgo data is on the verge of providing interesting astrophysical constraints. This suggests that the next generation of detectors should provide quick detections, and we explore this prediction in the next section.

2.3 Advanced LIGO/Virgo

We now calculate the expected detection rate of short GRB progenitors in the advanced LIGO and Virgo detectors, as well as additional detectors in Japan (KAGRA)[1] and India (LIGO-India)[2]. The advanced LIGO detectors are expected to begin operation in ~ 2015, and it is hoped that the LIGO and Virgo observatories will achieve their target advanced detector sensitivities by ~ 2017, with the Japanese [J] and Indian [I] detectors operating at comparable sensitivities by ~ 2020. We assume an identical noise curve for each of these

1. gwcenter.icrr.u-tokyo.ac.jp/en/

2. www.gw-indigo.org/tiki-index.php

Network	$\bar{V}(\mathrm{Gpc}^3)$	T_{first}	$\theta_j = 10^\circ$	$\theta_j = 30^\circ$	$\theta_j = 90^\circ$
HL(no SRM)	0.023	1.00	15	1.7	0.23
HLV(no SRM)	0.039	0.59	26	2.9	0.39
HLV	0.076	0.31	50	5.6	0.76
HLVJ	0.11	0.21	74	8.4	1.1
HLVI	0.11	0.20	75	8.5	1.1
HLVJI	0.16	0.15	103	12	1.6

Table 2.1: Mean detectable volume and wait times for the detection of binary coalescence associated with short GRBs in future GW detector networks. The network SNR is taken to be 10, and the volume is calculated for a $1.4\,M_\odot$–$1.4\,M_\odot$ binary. T_{first} is the waiting time until first detection (90% of cases), scaled to the value for the "no SRM" HL network (1.8 months for $\theta_j = 10^\circ$; 16 months for $\theta_j = 30^\circ$). The last three columns list the predicted event rate (per year) for three different values of the beaming angle.

instruments, given by the representative advanced LIGO noise curves in LIGO document T0900288-v3,[3] with $f_{\mathrm{low}} = 10\,\mathrm{Hz}$. We take the target design sensitivity to be given by the `ZERO_DET_high_P.txt` curve, corresponding to zero-detuning of the signal recycling mirror, and high laser power. We also consider an early, less sensitive incarnation of the detectors resulting from the absence of signal recycling mirrors, given by the `NO_SRM.txt` curve.

We calculate the mean detectable volume, $\bar{V}$, of a variety of ground-based networks. Our results are presented in Table 2.1, where in all cases we have assumed a network SNR threshold of $\rho = 10$, and our sources are taken to be equal-mass binaries with $m_1 = m_2 = 1.4\,M_\odot$. The mean detectable volume of a network is expected to scale as $\mathcal{M}^{5/2}$, with $\mathcal{M} = (m_1 m_2)^{3/5}/(m_1 + m_2)^{1/5}$ the chirp mass, although this relation is imperfect since the scaling also depends on the shape of the noise curve. For example, sufficiently massive binaries merge below the seismic noise floor of the detectors, and are undetectable. We note that the addition of the signal recycling mirror increases the detectable volume by a factor of two, resulting primarily from the increased sensitivity in the $\sim 200\,\mathrm{Hz}$ range.

The rate of binary coalescences is a function of the rate of observed GRBs (in gamma

3. dcc.ligo.org/cgi-bin/DocDB/ShowDocument?docid=2974

rays), $\mathcal{R}_{\rm GRB}$, the detectable volume, $\bar{V}$, and the beaming of the GRBs, θ_j, and is given by

$$\lambda = \bar{V}\mathcal{R}_{\rm GRB}/(1-\cos\theta_j). \tag{2.1}$$

As mentioned above, we assume $\mathcal{R}_{\rm GRB} = 10\,{\rm yr}^{-1}{\rm Gpc}^{-3}$. The predicted event rates as a function of beaming angle are presented in Table 2.1. In Fig. 2.1 we plot these results for the HL and HLV networks; the plot can be straightforwardly rescaled to different values of $M_{\rm total}$ and $\mathcal{R}_{\rm GRB}$. How long will a given network have to wait before seeing its first event? This is described by a Poisson process, with the probability of waiting a time τ before detecting the first event given by $e^{-\tau\lambda}$, for an event rate λ. We define $t_{\rm first}$ as the waiting time by which, in 90% of cases, the first event will have been observed: $t_{\rm first} = -\ln(0.1)/\lambda = 2.3/\lambda$. To convert to the 50% and 99% values, one multiplies the 90% waiting times by 0.3 and 2, respectively. The waiting times are presented in Table 2.1, scaled to the HL (no SRM) value (1.8 months for $\theta_j = 10^\circ$). The HLVJI network, with all detectors at the advanced zero-detuning high laser power sensitivity, has a waiting time that is a factor of 0.15 that of the HL (no SRM) curve; this works out to 8 days for $\theta_j = 10^\circ$ and 72 days for $\theta_j = 30^\circ$. If the GRB progenitors are larger mass systems, the waiting time is correspondingly shortened. It is to be noted that our results are roughly consistent with the completely independent rate estimates from population synthesis and observed binary pulsars (Abadie et al., 2010a).

Alternatively, the binary origin of short GRBs would be under pressure if no coalescences were observed within a sufficient amount of time. If we take a conservative upper limit of $\theta_j = 45^\circ$, we find that the binary origin can be falsified at the 99% level in 70 months for HL (no SRM), and in 21 months for HLV. However, even if short GRBs are not the result of binary mergers, we nonetheless expect a population of merging systems, and these should be observable by future observatories (Abadie et al., 2010a). The binary origin of short GRBs would also be ruled out by direct observation of a sufficiently nearby GRB without the detection of attendant GWs.

2.4 Triggered versus Untriggered

An important question when considering the future GW detection of binary mergers associated with short GRBs is whether triggered or untriggered detections are more likely. We assume that when a binary merges it emits both GWs and gamma rays. If the gamma-rays happen to point at the Earth, we will see the event as a gamma-ray burst; we call this a GRB triggered event. This improves the sensitivity of the GW search, as it reduces the need to marginalize over an unknown time and sky position. In addition, because the gamma-rays are thought to be beamed, a GRB triggered source is expected to be almost face-on, thereby increasing the strength of the signal in GWs when compared with a source with a random inclination. Alternatively, if the initial detection happens only in GWs, we call this an untriggered event. Given a fixed observed GRB rate, for small beaming angles the rate density of GRB progenitors increases (approaching ∞ as $\theta_j \to 0$), ensuring that for sufficiently small beaming the untriggered rate dominates over triggered GRBs.

In the previous section we calculated the waiting time and event rates for untriggered observations of GRB progenitor systems. We now consider the equivalent calculation in the case of a GW binary with a GRB trigger. If we assume the gamma-ray emission is uniform within θ_j, then the inclination of the binary, as far as the GW emission is concerned, will range uniformly in $\cos(\theta)$ from $\theta = 0^\circ$ (face-on) to $\theta = \theta_j$ (at the edge of the gamma-ray emission). For $\theta_j = 10^\circ$ the detectable volume, and thus the rate, are improved by a factor of 3.4, while for $\theta_j = 30^\circ$ the improvement is 2.8. The improvement in the rate for a perfectly face-on binary is 3.5.

We now estimate the reduction in SNR threshold due to the known time and sky position of the source (Dalal et al., 2006). The false alarm rate is related to the number of templates needed to search the data for the desired waveforms, and we therefore assume $\exp(-\rho^2/2) \propto 1/\#$ of templates (Biswas et al., 2009), where in the untriggered case we took $\rho = 10$. If we take this threshold to have been based on roughly one year of observation, the existence

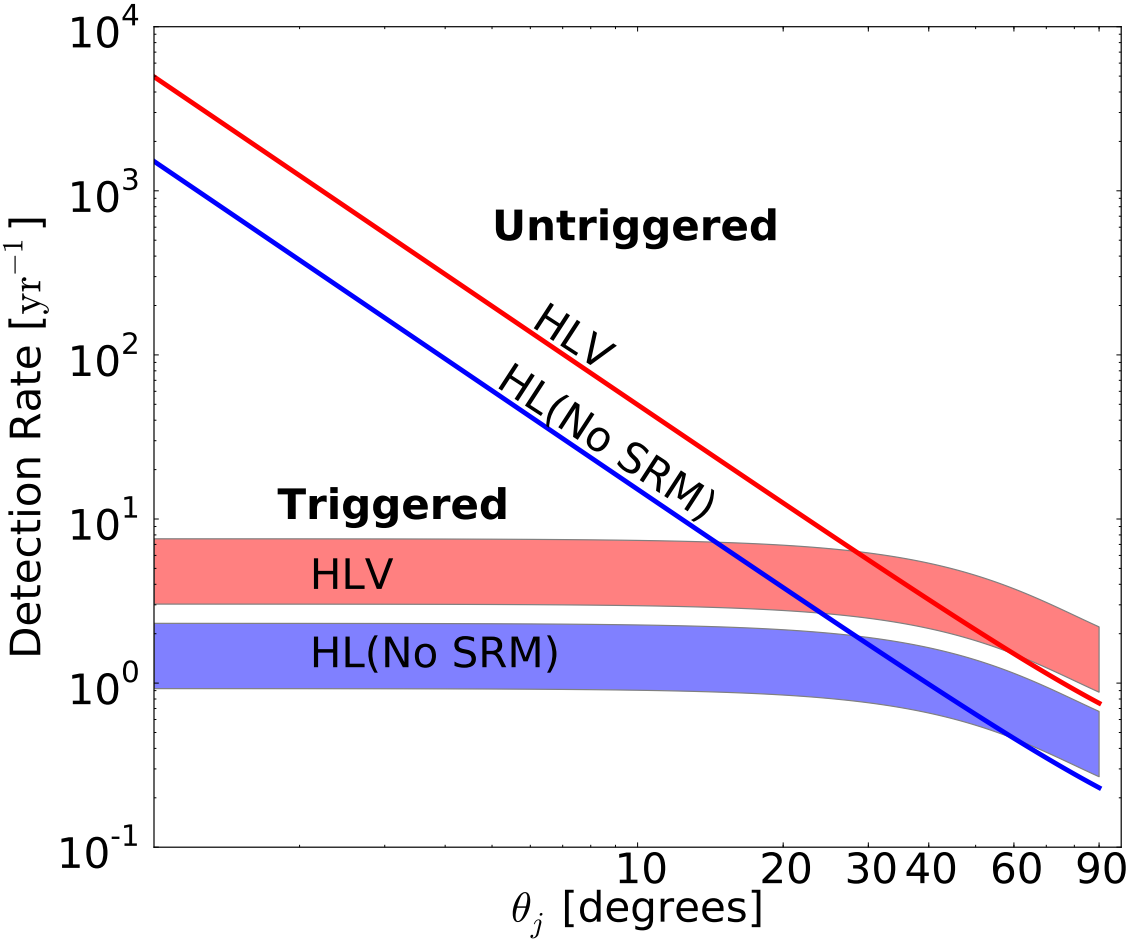

Figure 2.1: Predicted detection rate as a function of the beaming angle, θ_j. Results are shown for both untriggered and triggered GW observations of GRB progenitors, where we have assumed the observed local short GRB rate is $\mathcal{R}_{\rm GRB} = 10\,{\rm yr}^{-1}{\rm Gpc}^{-3}$. We plot results for two different GW networks: LIGO Hanford+Livingston (HL) operating without a signal recycling mirror (a potential early sensitivity), and Hanford+Livingston+Virgo (HLV) operating at the design sensitivity. Even in the pessimistic case (HL, no SRM, all short GRBs are beamed with $\theta_j = 30^\circ$), more than 1 detection per year is expected. For more substantial GW networks and reasonable beaming angles, the rates approach ~ 50 per year, implying a first detection within a month of operation. The bands show the detection rates for GRB triggered GW observations, for a range of values of the reduced SNR threshold (due to the presence of a trigger; see text). The rates of triggered and untriggered GW observations of GRBs match at $\theta_j \sim 30^\circ$ for $\rho \sim 7.5$. For lower values of θ_j untriggered observations occur more frequently than those triggered by GRBs, in which case the first observed binary GRB progenitors would be expected to be seen solely in GWs.

of a GRB trigger now reduces the observational window down to $\sim 10\,\mathrm{sec}$, for a reduction in the number of templates by a factor of $\sim 10^6$. If the sky localization in the untriggered case is $\sim 5\,\mathrm{deg}$ (Nissanke et al., 2011), then compared to a full-sky search ($41,253\,\mathrm{deg}^2$), the reduction in number of templates is a factor of $\sim 10^3$. The total number of templates is down by a factor of 10^9, which for the equivalent false alarm rate would imply that the SNR threshold is reduced to $\rho \sim \sqrt{(}-2\log(\exp(-10^2/2)\times 10^9)) = 7.7$.

In Fig. 2.1 we compare the detection rates for untriggered and triggered GRBs. We find that the rates of triggered and untriggered events are similar if the average GRB beaming angle is $\theta_j \sim 30^\circ$. This result is independent of the network configuration, the individual noise curves, and the assumed GRB rate, and is weakly dependent on the specific value of the threshold improvement due to the reduced number of templates (see the bands in the figure). If the GRBs are beamed at $\theta_j = 10^\circ$ or less, then the detected rate of untriggered GRBs is at least an order of magnitude larger than the rate of triggered sources. These estimates assume that the GRBs are being detected throughout the sky. If this isn't the case (e.g., the Swift BAT only sees 1/9 of the sky), the rates in the triggered case are further suppressed.

It is to be noted that this process can be inverted, and the wait time before first detection (and in between the first few detections) may be used to infer the beaming angle of GRBs. In addition, the relative rates of triggered and untriggered GRBs will help establish the beaming, and will be an important consistency test when compared with explicit determinations of the beaming distribution based on GW measurements of the inclination of GRB sources and jet break measurements in the electromagnetic spectrum.

As discussed above, recent observations have measured short GRBs with $\theta_j \lesssim 10^\circ$, indicating that it is likely that the detection rate of untriggered GRBs will be significantly greater than the rate of triggered ones, and implying that the first detection of a binary system which is a progenitor of a short GRB will not be triggered by a GRB. Although triggered

GRBs may be less frequent than untriggered ones, multi-messenger observations of these systems holds tremendous scientific potential, and should be aggressively pursued (Bloom et al., 2009).

2.5 Discussion

We have explored the connection between the observed short GRB rate, the beaming angle of short GRBs, and the predicted rate of detectable binary systems associated with progenitors of GRBs in networks of gravitational-wave observatories. We have shown that existing LIGO/Virgo data provides preliminary constraints on the beaming angle and mass distribution of short GRB progenitor systems. For example, we find that short GRB progenitors with mass $M_{\rm total} > 20\,M_\odot$ (uniformly distributed in component mass) and with beaming angles of $\theta_j < 4^\circ$ are ruled out by existing LIGO/Virgo data. These constraints, while novel, are fully consistent with our current understanding of the short GRB engine and rates.

We have analyzed the observed rate of short GRB progenitors in future networks of GW detectors. We find that, even in the case of only two detectors (HL) operating at conservative sensitivity, in 90% of cases we would expect a first detection of a binary within 16 months if the GRBs are beamed within $\theta_j = 30^\circ$, and within 55 days if $\theta_j = 10^\circ$. The expected event rates are $1.7\,{\rm yr}^{-1}$ ($\theta_j = 30^\circ$) and $15\,{\rm yr}^{-1}$ ($\theta_j = 10^\circ$). We find that the HLV network operating at design sensitivity would shorten these times to 4.9 months ($\theta_j = 30^\circ$) and 17 days ($\theta_j = 10^\circ$), with corresponding event rates of $5.6\,{\rm yr}^{-1}$ and $49\,{\rm yr}^{-1}$. Alternatively, the binary coalescence model for short GRB progenitors can be ruled out if an HLV network does not observe a binary within the first two years of observation.

Finally, we have shown that the rate of GRB triggered observations of GW systems associated with GRB progenitors is lower than the rate of untriggered observations if $\theta_j \lesssim 30^\circ$. This result is independent of network, noise curve, and GRB rate, and when coupled with recent observations of small beaming angles for short GRBs, suggests that the first

detections of GRB progenitors with advanced GW networks will not involve the observation of gamma rays from GRBs.

We conclude that, assuming short GRBs are the result of the merger of compact objects, and assuming that the resulting gamma-rays are beamed, the first detection of gravitational-waves from binary coalescence associated with a GRB progenitor will be untriggered, and may occur within weeks to months of operation of an early network of advanced sensitivity ground-based gravitational wave observatories.

CHAPTER 3

THE LOUDEST GRAVITATIONAL WAVE EVENTS

3.1 Introduction

Gravitational waves (GWs) couple very weakly to matter. The downside of this is that it took a century after they were first predicted by Einstein (Einstein, 1916) to directly detect them (Abbott et al., 2016; Abbott et al., 2016b). The upside is that GWs propagate with little interference, being almost impossible to absorb or scatter, and thus cleanly carry information from the source to the observer. As a result, both the amplitude and the measured signal-to-noise ratio (SNR) of GWs scale inversely with the luminosity distance to the source, leading to a universal SNR distribution of GW events as a function of the SNR detection threshold (Schutz, 2011). This follows directly from the simple relationship between distance and volume, and applies so long as the Universe can be approximated as Euclidean and the source population does not evolve with distance.

In the next few years of Advanced LIGO/Virgo operations we expect to have tens to hundreds of detections per year of gravitational waves from compact binary coalescences (Abbott et al., 2016c,a,b). These detections must follow the universal SNR distribution, and this offers an important internal self-calibration of the GW detector network. Additionally, the distribution offers a simple internal test of whether the first events are statistically consistent with expectations. Although most of these detections will be found with SNRs close to the detection threshold, there will exist a tail to higher SNR. Noticeably, the first GW detection, GW150914, was approximately two times louder than the detection threshold (Abbott et al., 2016). Fisher matrix calculations show that the timing, chirp mass, and amplitude measurement all improve as $\sim 1/\mathrm{SNR}$ (Cutler & Flanagan, 1994; Aasi et al., 2013). The highest SNR events will likely offer the best constraints on both intrinsic and extrinsic parameters of their sources, and thereby enable important physics and astrophysics. For example, accu-

rate determination of binary masses helps distinguish between neutron stars and stellar mass black holes, and elucidates the "mass gap" problem (Bailyn et al., 1998; Belczynski et al., 2012; Littenberg et al., 2015), while higher SNR measurements of the gravitational waveforms may help probe the neutron star equation-of-state (Bauswein & Janka, 2012; Hebeler et al., 2013; Takami et al., 2014). These loudest events are likely to have improved sky localization (Chen & Holz (2015) or see Chapter 4), increasing the probability of observing electromagnetic (EM) counterparts to the GW events and leading to the birth of GW/EM multi-messenger astronomy (Metzger & Berger, 2012). In particular, joint detections would confirm binary systems as the progenitors of short-hard gamma-ray bursts (Abadie et al., 2012b; Berger, 2011), probe the Hubble constant, and potentially measure the dark energy equation of state (Schutz, 1986; Holz & Hughes, 2005; Dalal et al., 2006; Nissanke et al., 2013a). We argue that these loudest events *must* exist, and will play an important role in the coming age of gravitational-wave astrophysics.

3.2 The Universal SNR Distribution

A given GW network will detect some number of GW events, with each event characterized by a measured SNR, ρ. We are interested in the distribution of ρ. We assume that the space density and intrinsic properties of the source population do not evolve. This is justified given that in the first few observing runs, the Advanced LIGO/Virgo network is only able to probe nearby universe (Abbott et al., 2016a). For the sake of definiteness and to enable Monte Carlo comparisons, in what follows we will assume that the GW sources are merging compact binaries, although our results are independent of this assumption and are valid for any discrete distribution of sources. We calculate the root-sum-square of the optimal matched filter signal-to-noise ratio, ρ_i, at each detector i:

$$\rho_i^2 = 2[F_+^2(\theta,\phi,\psi)^2 + F_\times^2(\theta,\phi,\psi)^2] \int \frac{|\tilde{h}(f)|^2}{S_h(f)}\, df, \tag{3.1}$$

where $\tilde{h}(f)$ is the Fourier transform of the waveform in the frequency domain, which is a function of the source luminosity distance $D_{\rm L}$, the binary inclination ι, and the binary's physical parameters such as the mass, spin, and precession. $S_h(f)$ is the detector power spectral density. F_+ and $F_\times$ are the detector antenna power patterns, which are themselves functions of the source's sky location (θ, ϕ) and orientation ψ. We then define the network SNR ρ as the root-sum-square of the SNR at each detector.

As the amplitude of the waveform $|\tilde{h}(f)|$ scales inversely as the luminosity distance to the source, so does the SNR; we note that this is true for *all* GW sources, not just for binary coalescences (e.g., Thorne (1987a)). The other extrinsic parameters (sky location, binary orientation, and inclination) are randomly distributed and do not impact the final distributions, as shown explicitly below. The probability of a merger lying within an infinitesimal interval dD near the comoving distance D is given by $f_D dD \propto D^2 dD$, where $f_D = f(D)$ is the distribution of the source comoving distance. In the nearby universe we can approximate the luminosity distance by the comoving distance. If we assume that the mass distribution and the space density do not evolve with distance, then the resulting distribution of SNR only depends upon the distance. We find

$$f_\rho = f_{D_L} \left| \frac{dD_L}{d\rho} \right| = f_D \left| \frac{dD}{d\rho} \right| \propto \frac{1}{\rho^2} \frac{1}{\rho^2} = \frac{1}{\rho^4}.$$

where the second equality is only true at low redshift. Normalizing this for a given network SNR threshold, $\rho_{\rm th}$, we find that the distribution of SNRs for sources in the local universe is exactly described by

$$f_\rho = \frac{3\rho_{\rm th}^3}{\rho^4}. \tag{3.2}$$

This is identical to Eq. 24 of Schutz (2011).

In Fig. 3.1 we plot this distribution assuming $\rho_{\rm th} = 12$. The distribution peaks at the threshold value, and has a tail to higher SNR events. For explicit comparison we have also

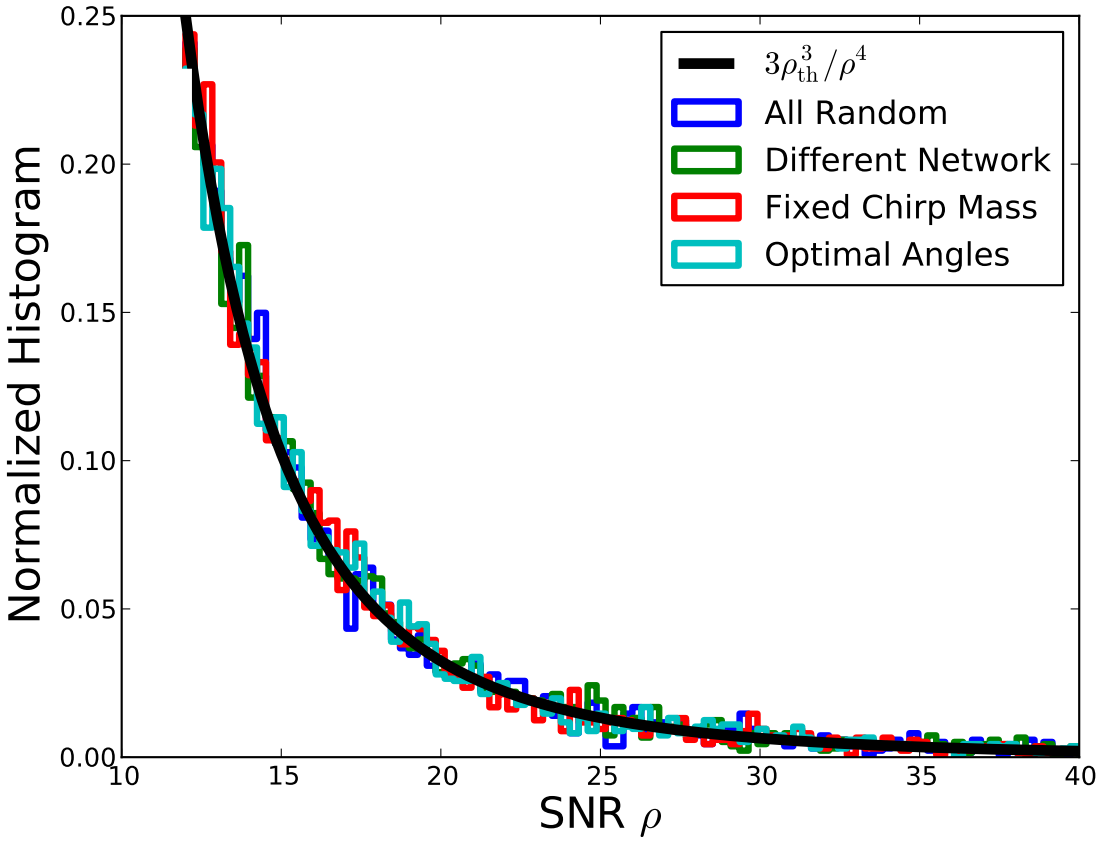

Figure 3.1: Universal distribution of SNR (Eq. 3.2), for $\rho_{\rm th} = 12$, plotted as the solid black curve. The colored histograms show the results from our Monte Carlo simulations of 5,000 detections. "All Random" is from the basic simulation described in the text, and verifies our analytic prediction. The results are independent of the network properties ("Different Network" has a different number of detectors, with different relative orientations and noise curves), the chirp mass distribution ("Fixed Chirp Mass"), and the sky location and inclination distribution ("Optimal Angles" has all binaries "overhead" and face-on). This shows explicitly that the SNR distribution is universal.

performed Monte Carlo simulations of the detection of a binary population, sampling over the full parameter space $(D_L, \theta, \phi, \psi, \iota)$ with random sky locations and binary orientations, and with the total mass of the binaries, $M_{\rm tot} = m_1 + m_2$, drawn uniformly between $2M_\odot$ and $20M_\odot$ and m_1 drawn uniformly between $1M_\odot$ and $M_{\rm tot} - 1M_\odot$. For each randomly drawn binary we use Eq. 5.1 to calculate the SNR of the simulated events for a given GW network. As shown in Fig. 3.1, the histograms of SNR for our various simulated populations follow our predictions. The distribution of SNR presented in Eq. 3.2 is universal, and is what will be found in all GW detectors for all non-evolving, low-redshift GW source populations.

3.3 The Universal Loudest Event Distribution

We now turn our attention to the high-SNR tail of events, and make predictions for the highest SNR event out of any detected sample of GW events. We assume that within any arbitrary GW network we have N compact binary detections with SNR values given by $\{\rho_1, \rho_2, ..., \rho_N\}$. We define the loudest event as $\rho_{\rm max} = \max\{\rho_1, \rho_2, ..., \rho_N\}$. The probability of $\rho_{\rm max}$ being less than a given value ρ is

$$\begin{aligned} P(\rho_{\rm max} < \rho) &= P(\rho_1 < \rho; \rho_2 < \rho; ...; \rho_N < \rho) \\ &= P(\rho_1 < \rho) P(\rho_2 < \rho) ... P(\rho_N < \rho) \\ &= (F_\rho)^N, \end{aligned}$$

where the second line follows from the assumption that each event is independent. F_ρ is the cumulative distribution function of ρ and can be computed by integrating Eq. 3.2 from $\rho_{\rm th}$ to any desired value of ρ. $P(\rho_{\rm max} < \rho)$ is equivalent to the cumulative distribution function, $F_{\rho_{\rm max}}$, of the loudest event, $\rho_{\rm max}$. The probability distribution function of the loudest event,

$f_{\rho_{\rm max}}$, is obtained by taking a derivative:

$$f_{\rho_{\rm max}} = \frac{dF_{\rho_{\rm max}}}{d\rho_{\rm max}} = \left.\frac{d(F_\rho)^N}{d\rho}\right|_{\rho=\rho_{\rm max}}$$
$$= \frac{3N}{\rho_{\rm max}}\left(\frac{\rho_{\rm th}}{\rho_{\rm max}}\right)^3\left[1-\left(\frac{\rho_{\rm th}}{\rho_{\rm max}}\right)^3\right]^{N-1}. \quad (3.3)$$

We have verified this distribution explicitly using Monte Carlo techniques. See Vallisneri (2012) for an alternative approach to deriving this distribution.

We are now able to forecast the distribution of the loudest events, as shown in Fig. 3.2. The probability that the loudest event is louder than ρ, out of N detections above a detection threshold $\rho_{\rm th}$, is given by $P(\rho_{\rm max} > \rho)$, and can be calculated by integrating Eq. 3.3 from ρ to infinity. For example, if we set the network detection threshold to $\rho_{\rm th} = 12$ (appropriate for the case of Advanced LIGO/Virgo) we find that 90% of the time the loudest event out of the first 4 detections will have $\rho_{\rm max} > 15.8$. This has already been verified by the first two gravitational-wave detection in the first Advanced LIGO observing run (Abbott et al., 2016b). The loudest event out of the first 40 detections, corresponding roughly to the expected number of detections in the third Advanced LIGO/Virgo observing run (Abbott et al., 2016b), will have $\rho_{\rm max} > 31$. Half the time we will find the loudest event to have $\rho > 22$ for 4 events and $\rho > 47$ for 40 events. We emphasize that these statements are independent of the specific noise curves or configurations of the detector network or even the nature of the source population.

The distribution of the loudest events given in Eq. 3.3 depends upon only two parameters: the number of detections, N, and the detection threshold, $\rho_{\rm th}$. Since the shape of the distribution is similar for all N and $\rho_{\rm th}$, we are able to find a scaling to produce a universal distribution. We define a new variable, $y \equiv \rho_{\rm max}/a$, where a is an arbitrary scaling. The

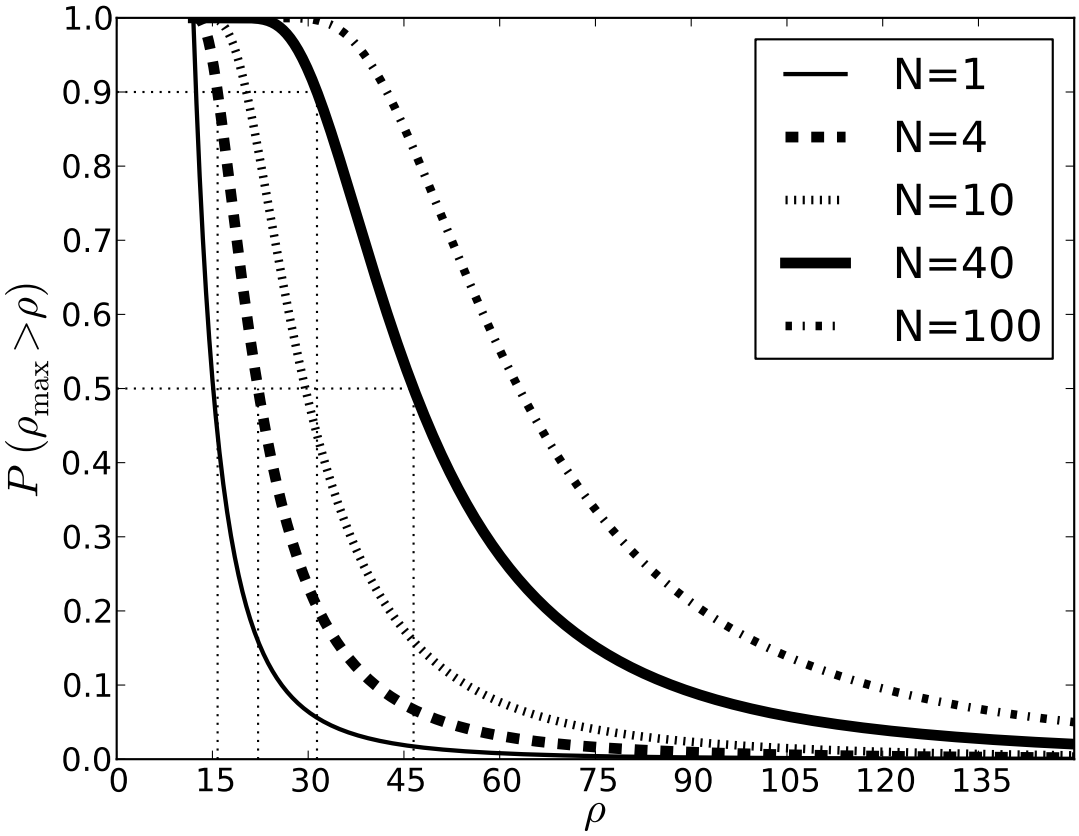

Figure 3.2: Probability that the loudest event of a given sample of detections has SNR greater than ρ. We take the network threshold to be $\rho_{\rm th} = 12$, and we assume samples sizes of $N = 1$, 4, 10, 40, and 100 detections. We find that in 90% of cases the loudest event among the first four detections ($N = 4$) will be louder than $\rho_{\rm max} = 15.8$, while 50% of cases will have a loudest event with $\rho_{\rm max} > 22.2$. For a sample of 40 detections these rise to $\rho_{\rm max} > 31$ (90%) and $\rho_{\rm max} > 47$ (50%). Notice that the $N = 4$ curve is visibly shifted from the $N = 1$ case, implying that the loudest event out of a small number of detections can be significantly louder than a typical "threshold" event.

distribution of y values becomes

$$f_y = \frac{d\rho_{\max}}{dy} f_{\rho_{\max}} = a\frac{3N}{ay}\frac{\rho_{\rm th}^3}{a^3y^3}\left[1-\frac{\rho_{\rm th}^3}{a^3y^3}\right]^{N-1}.$$

If we set $a = \rho_{\rm th}N^{1/3}$ this distribution becomes

$$f_y = \frac{3}{y^4}\left[1-\frac{1}{Ny^3}\right].$$

We note that this distribution is independent of $\rho_{\rm th}$ and N when N is large. In Fig. 3.3 we explicitly show that this scaling produces a universal form for the distribution of the loudest events. Furthermore, from this distribution we are able to produce generic, simple, and powerful statistical predictions. For example, we conclude that in 90% of cases, $\rho_{\max} > 0.76\rho_{\rm th}N^{1/3}$, while in 50% of cases, $\rho_{\max} > 1.13\rho_{\rm th}N^{1/3}$. Comparing to the exact analytic form, these expressions are good to 8% for 4 detections and 0.6% for 40 detections.

3.4 The SNR Distribution in Individual Detectors

In Eq. 3.2 we show the distribution of SNR for an arbitrary detector network, where the network SNR is the root-sum-square of the SNRs in each individual detector comprising the network. In addition to the overall source amplitude, the signal strength in each detector depends on the individual detector's sensitivity and the relative orientation between the source and each detector. For a detector network with a given network threshold, the distribution of SNR in each *individual* detector can be calculated:

$$f_{\rho_i} = \int_{\rho_i \geq \rho_{\rm eff}} f(\rho_i|\theta,\phi,\psi,\iota)\, f_{\rm det}(\theta,\phi,\psi,\iota)\, d\theta d\phi d\psi d\iota \tag{3.4}$$

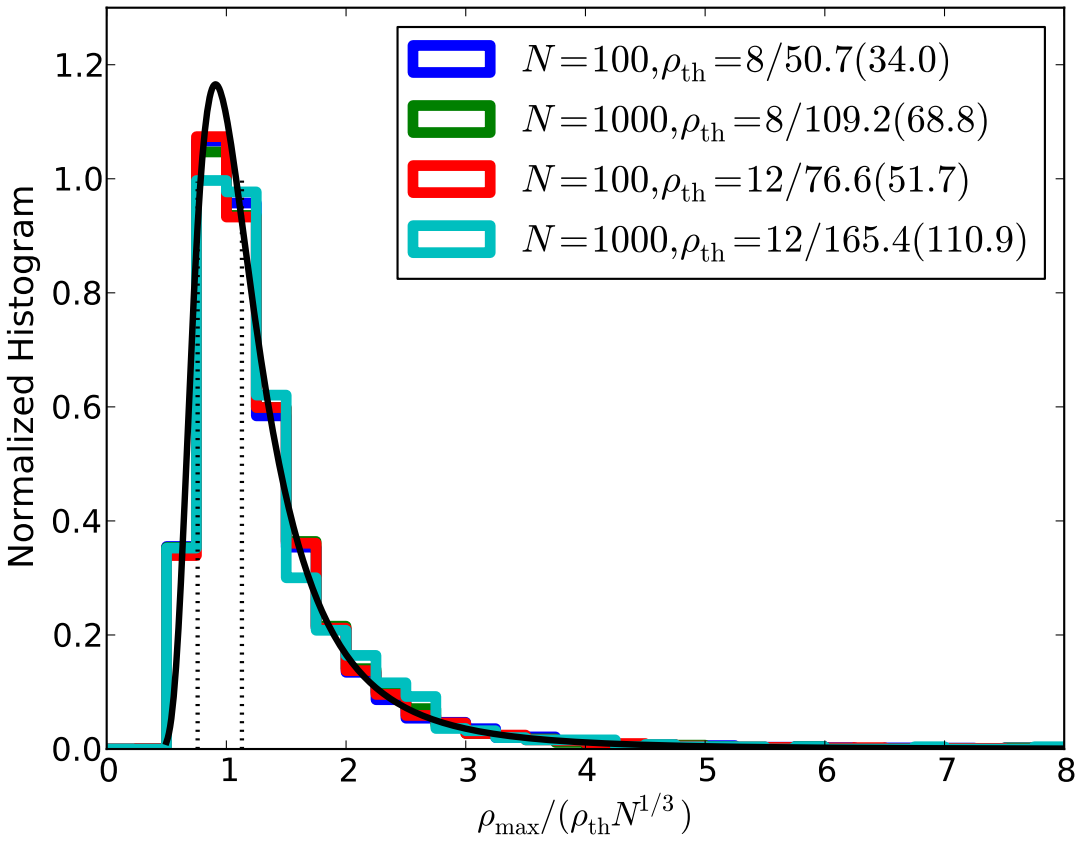

Figure 3.3: Rescaled histogram of $\rho_{\rm max}/(\rho_{\rm th}N^{1/3})$ from $N = 100$ and $N = 1,000$ detections, repeating each random sample ten thousand times, and with $\rho_{\rm th}$ taken to be 8 or 12. The average and standard deviation of $\rho_{\rm max}$ before rescaling are shown in the legend for reference. In all cases the distributions of $\rho_{\rm max}$ follow a similar shape after rescaling. For 90% of the cases (left vertical dotted line), $\rho_{\rm max} > 0.76\rho_{\rm th}N^{1/3}$, while for 50% of the cases (right dotted line), $\rho_{\rm max} > 1.13\rho_{\rm th}N^{1/3}$.

where $f(\rho_i|\theta,\phi,\psi,\iota) = 3\rho_{\rm eff}^3/\rho_i^4$ and

$$\rho_{\rm eff} \equiv \rho_{\rm th}/\left(\sum_{j=1}^{N} R_{ji}\right)^{1/2}$$

with $R_{ji} \equiv \rho_j^2/\rho_i^2$. The prior on sky location and binary orientation depends upon the antenna power pattern, P_j (Schutz, 2011):

$$f_{\rm det}(\theta,\phi,\psi,\iota) = \frac{1}{n}\left(\sum_{j=1}^{N} P_j\right)^{3/2} \sin\theta\,\sin\iota,$$

where the normalization factor n is integrated over $d\theta\,d\phi\,d\psi\,d\iota$. We simplify Eq. 3.4 by rewriting the individual SNR, ρ_i, as $y_i \equiv \rho_i/\rho_{\rm th}$. We assume each detector has identical (arbitrary) sensitivity, finding:

$$f_{y_i} = \frac{3}{n}\int_{\sum_{j=1}^{N} R_{ij} \geq \frac{1}{y_i^2}} \frac{1}{y_i^4}\, P_i^{3/2} \sin\theta\,\sin\iota\,d\theta\,d\phi\,d\psi\,d\iota. \tag{3.5}$$

This expression gives the distribution of SNR detected by each individual detector as part of a given detector network. In Fig. 3.4 we show the SNR distribution for each detector within a network composed of two (LIGO-Hanford [H] and LIGO-Livingston [L]) and three (H,L, and Virgo [V]) detectors. For any two detector network, the SNR distributions for the individual detectors will be identical if the detectors operate at the same sensitivities. We find that Virgo tends to detect lower SNR values compared to the LIGO detectors when operated within the HLV network, even if the sensitivities of all three instruments are comparable. This is because the H and L detector arms are more closely aligned, and therefore more sources will be detected in the optimal directions for H and L ("overhead" for those detectors), leading to weaker SNR in Virgo.

We note that in practice GW searches often use a complicated detection threshold to

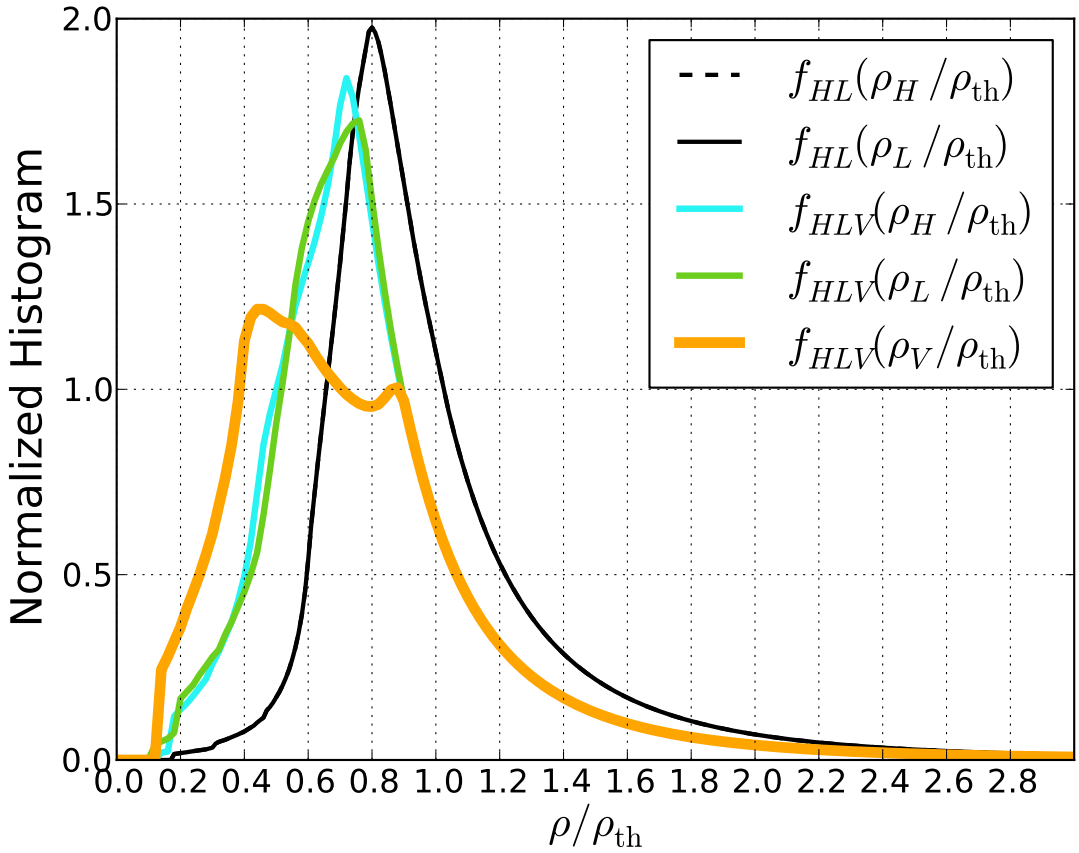

Figure 3.4: Scaled SNR distributions for individual detectors as part of an HL or HLV network, for identical detector sensitivities. These distributions are universal and can be applied for any network threshold. Note in particular that the Virgo detector finds lower SNR values than the LIGO detectors, even when all are operating at equivalent sensitivity.

better handle the presence of non-Gaussian noise (i.e., glitches). To get a sense of the importance of this, we have implemented a combined coherent/coincident threshold approach, where we demand $\rho_{\rm net} > 12$ and also implement an individual threshold of $\rho_i > 5$ in at least two detectors. We find that this additional restriction eliminates less than 1% of events in the HLV network, and therefore does not substantially impact any of our predicted SNR distributions.

3.5 Discussion

Bernard Schutz has emphasized that there exists a universal distribution of SNR that will be measured for gravitational wave sources (Schutz, 2011). This distribution is presented in Eq. 3.2, and assumes only that the sources are local and the spatial density of the sources does not evolve; it makes no assumptions about the nature of the sources (e.g., binary coalescences or supernovae or something else entirely), the properties of the sources (e.g., mass distribution of binaries, inclination distribution, sky locations), or the properties of the GW network (e.g., pulsar timing arrays or interferometers of any number, sensitivity, or location [including ground or space]). We have derived the universal distribution for the loudest (highest SNR) events, for any given number of detected events. When there are N detections above network threshold $\rho_{\rm th}$, 90% of the time the loudest event will have SNR larger than $0.76\rho_{\rm th}N^{1/3}$. This loudest event may play an important role in binary parameter estimation and multi-messenger astronomy, as it is expected to be particularly well localized on the sky (2D) and in space (3D) (Chen & Holz (2015, 2016) or see Chapters 4 and 5). If we consider the first four detections by the Advanced LIGO network (or any sources within any network with a network threshold of $\rho_{\rm th} = 12$), we find that half the time the loudest event will be louder than $\rho = 22$, and the localization area will shrink by a factor of ~ 3 compared to threshold events. The particularly high SNR and good localization of GW150914 have already verified this prediction (Abbott et al., 2016).

Our results are similar to the $V/V_{\rm max}$ test, which is a geometric test used for electromagnetic astronomical sources (Schmidt, 1968). For any population of sources, one calculates the volume enclosed by the distance to each individual source, V, and the maximum volume to which that source could have been observed, $V_{\rm max}$. If there is no evolution in the source population, simple geometric arguments imply that the observed values of $V/V_{\rm max}$ must be uniformly distributed between 0 and 1. The same test can be applied to non-evolving GW sources at low redshift: since SNR scales inversely with D, and since volume scales as

D^3, we find $V/V_{\rm max} \sim (D/D_{\rm max})^3 \sim (\rho_{\rm th}/\rho)^3$ distributes uniformly between 0 and 1. We have focused on the SNR distribution instead, since this quantity is directly measured by GW detectors. However, the $V/V_{\rm max}$ distribution remains true to arbitrary redshift (modulo gravitational lensing, which adds noise and may also introduce magnification bias to all high-z distributions). This is not true for the SNR distributions discussed above, since at high redshift two additional effects come in: (1) luminosity distance (which sets the SNR) and comoving distance (which is relevant for the comoving volume) start to deviate from each other, and (2) the source redshift affects where the source is found relative to the frequency response of the GW detectors. Both of these effects break the universality of the SNR distributions. The latter effect depends upon properties of the source population and detector noise curves; for binary systems the effect is encapsulated in the redshift dependence of I_7. For example, using the Einstein Telescope noise curve (Hild et al., 2008) we find a $\sim 10\%$ suppression from the form in Eq. 3.2 for binary neutron stars detected at $\rho_{\rm th} = 12$ (corresponding to a horizon of $z \sim 1.2$). This effect grows to 25% and 60% as the binary masses increase to $3M_\odot$–$3M_\odot$ and $10M_\odot$–$10M_\odot$, respectively (corresponding to horizons of $z \sim 2.8$ and $z \sim 4.8$). In principle, precise measurements of the distribution of SNR could be used to infer the intrinsic mass distribution of binary systems, as well as probe the cosmological parameters by measuring directly the evolution of the cosmological volume. In practice the evolution in the rate density of the source populations dominates over the cosmological effects, and we are more likely to be able to measure the former than the latter.

These universal distributions are a robust prediction for all GW sources and for all GW networks, and therefore serve as an important internal consistency check for the detectors. For example, in LIGO's 6th and Virgo's 3rd science run there was a "blind" hardware injection event intended to test the data analysis procedures. This event is presented in Fig. 3 of Abadie et al. (2012c): the "false" coincidence events are found at SNR below 9.5, while the single injection event stands out at SNR of ~ 12.5. Given our universal distribution,

we can calculate the probability of having a single event at $\rho = 12.5$ with no other events down to a threshold of $\rho = 9.5$. Instead of the loudest event, we are now interested in the "quietest" event; following the approach in Eq. 3.3, we find that the distribution of the lowest SNR for N events is: $f_{\rho_{\rm min}} = 3N\,\rho_{\rm th}^{3N}/\rho_{\rm min}^{3N+1}$. For the blind injection we have $N = 1$, and the probability that the first event will have $\rho \geq 12.5$ when the threshold is $\rho_{\rm th} = 9.5$ is $(9.5/12.5)^3 = 44\%$. We conclude that the injection event was not unlikely, even in the absence of any other events down to $\rho = 9.5$ [1]. The first LIGO/Virgo events must follow statistical expectations from our universal distributions, and this will be an important sanity check.

In conclusion, all non-evolving low redshift populations found in all GW detectors must follow the SNR distribution presented in Eq. 3.2. This distribution serves as an important internal consistency check, and offers the opportunity to test instrumental calibration and sample completeness, as well as testing for source and cosmological evolution. In addition, we robustly predict the distribution of the loudest events. These events *must* be found, and will play an important role in gravitational wave astrophysics.

1. The SNR values presented in Abadie et al. (2012c) are based on a "reweighted" SNR statistic, rather than SNR of the form used in this chapter. Converting to the latter leads to values of $\rho \sim 24$ and $\rho_{\rm th} \sim 12$, leading to a probability $\sim (1/2)^3 = 13\%$.

CHAPTER 4

FACILITATING FOLLOW-UP OF LIGO-VIRGO EVENTS USING RAPID SKY LOCALIZATION

4.1 Introduction

Observations of a source in both the gravitational wave (GW) and electromagnetic (EM) spectrum would herald the much anticipated age of multi-messenger gravitational-wave astronomy. Although in some cases the EM sources may naturally be observed in coincidence with the GW signals (e.g., short gamma-ray bursts [GRBs]), the more common case is expected to consist of GW detection followed by EM exploration of the GW sky localization error boxes (Abbott et al., 2016c; Metzger & Berger, 2012; Chen & Holz, 2013). The most promising sources for ground-based GW instruments are binary inspirals and mergers of neutron stars and/or stellar-mass black holes. It is not known if these systems are accompanied by EM signatures, although there is growing evidence that short GRBs result from binary coalescence (Kocevski et al., 2010; Fong et al., 2013; Fong & Berger, 2013). These systems may also produce X-ray, radio, optical, and/or infrared afterglows, e.g. kilonovae powered by the radioactive decay of r-process elements (Berger et al., 2013; Tanvir et al., 2013; Freiburghaus et al., 1999; Metzger et al., 2010). There will be tremendous interest in identifying possible counterparts to LIGO sources. The success of these endeavors will depend crucially on the ability of the LIGO network to quickly and accurately localize GW sources on the sky.

The advanced LIGO detectors, Hanford [H] and Livingston [L], have completed their first observing run (Abbott et al., 2016b), and started their second observing run in Fall 2016, with the Virgo [V] detector potentially joining during the run (Acernese et al., 2015; Abbott et al., 2016a). GW source localization mainly relies on triangulation based on the arrival times of the GWs at the different sites of the detector network, as discussed in Fairhurst (2009, 2011),

as well as the relative phase and amplitude information. The ability to triangulate a source is crucially dependent upon the number, bandwidths, and separations of detectors in the GW network, as well as the signal-to-noise ratio (SNR) within each detector.

There are several existing pipelines to do sky localization of compact binary coalescences (CBCs) within LIGO data. The lowest latency pipeline is the BAYESTAR pipeline (Singer & Price, 2016) in LALInference, which utilizes the output of the LIGO CBC detection pipeline to directly estimate sky location. The detection pipeline produces rapid point estimates of such quantities as time of arrival, phase, signal-to-noise ratio (SNR), and chirp mass. The most accurate determination of the sky location comes from the full parameter estimation pipeline within LALInference (Veitch et al., 2015; Aasi et al., 2013). This entails fitting for the data + noise, utilizing Markov Chain Monte Carlo (MCMC) or nested sampling techniques to estimate the relevant parameters of the binary. Although this approach generates the most reliable values of parameters, including the best estimates of the sky position, it requires significant computational resources and can take hours, if not days or longer, to run.

In this chapter we present an extremely low latency (< 1 second after detection) localization algorithm incorporating the timing, phase, and SNR output from the detection pipeline to estimate the localization area. We take as input the relative timing and phase, and the SNR ratios of the GW detectors. From these parameters we estimate solely the localization area, marginalizing over all other parameters.

Our approach is very similar to BAYESTAR (Singer & Price, 2016; Singer et al., 2014), with a number of important differences: first, our sky localization algorithm utilizes the log of the SNR ratios, rather than the value of SNR at each detector. This obviates the need to infer the binary chirp mass or distance, saving the time of fitting for these parameters, only to marginalize over them afterwards. By taking the logarithm, the Gaussianity of the likelihood is approximately preserved. Second, we calculate the sky location prior from the antenna power patterns and the relative sensitivities of the detectors. This prior applies to all discrete

[1] sources detected by ground-based detector networks, and can be pre-calculated in advance of utilization of the pipeline. Finally, our algorithm explicitly marginalizes over only two unknown parameters: the binary orientation and inclination. Since this is a small parameter space, we can pre-grid the entire sky and pre-calculate this marginalization, allowing our localization algorithm to consist primarily of lookup tables and summation, rendering it simple and fast. Our alogrithm can be run in < 1 second on a laptop, offering the potential for real-time localization as the GW source evolves within the detectors. Since our method has been developed completely independently of the LIGO code efforts, it also provides a consistency check of the existing LIGO codebase (and in particular BAYESTAR).

We use our localization algorithm to explore issues related to EM follow-up. For example, we consider the dependence of the localization area as a function of SNR of the events, explicitly determining the expected improvement in localization from high-SNR events. The incidence of these high-SNR events can be predicted analytically, and depends solely on the measured event rate (Chen & Holz (2014) or see Chapter 3). This approach has been applied to the Dark Energy Camera follow-up event selection process, and was applied to the first two GW detections (Cowperthwaite et al., 2016; Soares-Santos et al., 2016). We show that EM priors on the inclination do not significantly help GW localization. We also discuss the potential of cross-correlating LIGO sources with other all-sky observatories, such as Fermi GBM, to dramatically improve sky localization.

4.2 Low Latency Localization Algorithm

The probability of a source being located at a sky position (θ, ϕ), given a set of observables $\vec{\epsilon}$, can be written as:

$$f(\theta, \phi|\vec{\epsilon}) = \frac{f(\vec{\epsilon}|\theta, \phi)\, f(\theta, \phi)}{f(\vec{\epsilon})}. \tag{4.1}$$

1. As opposed to stochastic and continuous sources, for which the prior does not apply.

The prior on source location can be estimated from the detector network's antenna power pattern (Sathyaprakash & Schutz, 2009; Schutz, 2011),

$$\Omega(\theta, \phi, \iota, \psi) = F_+^2(\theta, \phi, \psi)(1 + \cos^2 \iota)^2 + 4\mathrm{F}_\times^2(\theta, \phi, \psi)\cos^2 \iota, \tag{4.2}$$

and sensitivity,

$$I_7 = \int \frac{f^{-7/3}}{S_h(f)}\, df, \tag{4.3}$$

where ψ is the orientation of the binary within the plane of sky, ι is the inclination angle between the binary's rotation axis and the line of sight, and $S_h(f)$ is the detector's power spectral density. The prior can be calculated from:

$$f(\theta, \phi) = \int f(\theta, \phi, \iota, \psi)\, d\iota d\psi, \tag{4.4}$$

where

$$f(\theta, \phi, \iota, \psi) \propto \left(\sum_i \Omega_i(\theta, \phi, \iota, \psi)\, I_{7,i} \right)^{3/2} \sin\theta \sin\iota, \tag{4.5}$$

and where the sum goes over each detector in the network (i =H, L, V, ...). The likelihood function is expressed as a function of the sky location, (θ, ϕ), and the GW observables, $\vec{\epsilon}$:

$$f(\vec{\epsilon}|\theta, \phi) \propto \exp\left(-\Delta\chi^2_{\vec{\epsilon}}(\theta, \phi)/2\right) \tag{4.6}$$

where $\Delta\chi^2_{\vec{\epsilon}}$ can be calculated from a chi-square minimization process:

$$\Delta\chi^2_{\vec{\epsilon}}(\theta, \phi) = \chi^2_{\vec{\epsilon}}(\theta, \phi) - \chi^2_{\vec{\epsilon},\mathrm{min}}(\theta_{\mathrm{min}}, \phi_{\mathrm{min}}). \tag{4.7}$$

For our algorithm the observables are the arrival times of the signal, t_i, the phase, η_i, and the SNR, ρ_i, measured at each detector. If the SNR measurements are independent of the arrival times and phases, the chi-square expression can be separated: $\chi^2_{\vec{\epsilon}}(\theta, \phi) =$

$\chi^2_\zeta(\theta,\phi) + \chi^2_\rho(\theta,\phi)$, where ζ represents the contribution from arrival time and phase, and ρ represents the contribution from SNR (see below). We note that this assumption that ζ and ρ are independent is an approximation, since these quantities are coupled through their dependence on ι and ψ, and therefore our formalism is not perfectly Bayesian in accordance with Eq. 4.1. However, as described below, we show explicitly in Fig. 4.4 that our formalism is self consistent. We have also developed a fully Bayesian generalization of our approach, and find consistent results. We assume the errors in arrival time, phase, and SNR are Gaussian and independent between detectors. This appears to be a fair assumption (Berry et al., 2015), although our method can be generalized if the error properties are known.

The differences in the arrival time between detectors allows us to triangulate for the sky position of the source. Using only this information, every pair of detectors will localize the source to an annulus on the sky. Three detectors with two intersecting annuli will localize the source to two intersection regions, while four or more detectors can localize the source to a single distinct region. This technique has been discussed by Fairhurst (2009); Wen & Chen (2010); Fairhurst (2011) using a flat-sky approximation; we rederive these results in full generality.

The phase of a binary, η, at time t, measured in the ith detector is a function of the detector orientation, and the binary sky location, inclination, and orientation: $\eta(t) + \eta_i(\theta,\phi,\iota,\psi)$. Following Sathyaprakash & Schutz (2009), we find:

$$\eta_i(\theta,\phi,\iota,\psi) = \tan^{-1}\left(\frac{2F_{\times,i}(\theta,\phi,\psi)\cos\iota}{F_{+,i}(\theta,\phi,\psi)(1+\cos^2\iota)}\right). \tag{4.8}$$

By considering only the phase difference between detectors, we avoid needing to determine the absolute phase of the binary. The sky location remains degenerate with the inclination and orientation, and this can be subsequently marginalized over. There are additional phase differences due to the separation of the detectors on Earth; this can be inferred from the difference in signal arrival times. The phase and timing measurements are therefore

correlated.

We follow the approach of Grover et al. (2014); Fairhurst (2009, 2011) to estimate the timing and phase covariance matrix. These errors depend on the SNR and the detector effective bandwidth of the source, $\sigma_{\bar{f}}^2 = \bar{f^2} - (\bar{f})^2$:

$$\mathrm{cov}(t,\eta) \equiv \begin{bmatrix} \sigma_{tt}^2 & \sigma_{t\eta}^2 \\ \sigma_{\eta t}^2 & \sigma_{\eta\eta}^2 \end{bmatrix} = \begin{bmatrix} \frac{1}{(2\pi\rho\sigma_f)^2} & -\frac{\bar{f}}{2\pi\rho^2\sigma_f^2} \\ -\frac{\bar{f}}{2\pi\rho^2\sigma_f^2} & \frac{\bar{f^2}}{(\rho\sigma_f)^2} \end{bmatrix}, \tag{4.9}$$

where $\bar{f^n} = 4\int \frac{|\bar{h}(f)|^2}{S_h(f)} f^n \, df$. The error in *measured* arrival times and phases are expected to be distributed as a 2D Gaussian centered at the true value with covariance given by Eq. 4.9. In reality, the simulated binary neutron stars merger signals in Singer et al. (2014) follow a Gaussian distribution with a standard deviation that is 1.4 and 1.3 times larger in arrival time and phase, respectively. The difference in arrival times and phase between pairs of detectors is a linear function of the independent observables, t_i and η_i:

$$\begin{aligned} \Delta t_{ij} &\equiv t_i - t_j, \\ \Delta\eta_{ij} &\equiv \eta_i - \eta_j, \quad i,j = \mathrm{H,L,V,}\ldots \text{ with } i \neq j. \end{aligned}$$

Thus the *measured* timing and phase differences can still be described by 2D Gaussians. If there are N detectors in a given GW network, there are $N-1$ independent timing and phase differences. Without loss of generality we can denote one of the detectors as reference detector I, and define all time-of-arrival and phase differences with respect to this fiducial detector:

$$\begin{aligned} \Delta t_i &\equiv t_I - t_i, \\ \Delta\eta_i &\equiv \eta_I - \eta_i, \quad i \neq I. \end{aligned} \tag{4.10}$$

The chi-square value is:

$$\chi^2_\zeta(\theta,\phi,\iota,\psi) = \sum_{i,j} \zeta_i^T(\theta,\phi,\iota,\psi) V_{ij}^{-1} \zeta_j(\theta,\phi,\iota,\psi) \tag{4.11}$$

where

$$\zeta_i(\theta,\phi,\iota,\psi) \equiv \begin{bmatrix} \Delta t_i - \Delta t_i(\theta,\phi) \\ \Delta\eta_i - \Delta\eta_i(\theta,\phi,\iota,\psi) \end{bmatrix}$$

and V_{ij} is the covariance matrix. Since all the differences are in reference to the same detector I, any two differences are not independent.

Following Eq. 4.9, we find that when $i = j$ the components of V_{ij} are given by [2]:

$$\begin{aligned} \sigma^2_{\Delta t_i \Delta t_i} &= \sigma^2_{t_{\rm I} t_{\rm I}} + \sigma^2_{t_i t_i}, \\ \sigma^2_{\Delta\eta_i \Delta\eta_i} &= \sigma^2_{\eta_{\rm I}\eta_{\rm I}} + \sigma^2_{\eta_i\eta_i}, \\ \sigma^2_{\Delta t_i \Delta\eta_i} &= \sigma^2_{\Delta\eta_i \Delta t_i} = \sigma^2_{t_{\rm I}\eta_{\rm I}} + \sigma^2_{t_i\eta_i}. \end{aligned}$$

If $i \neq j$,

$$\begin{aligned} \sigma^2_{\Delta t_i \Delta t_j} &= \sigma^2_{t_{\rm I} t_{\rm I}}, \\ \sigma^2_{\Delta\eta_i \Delta\eta_j} &= \sigma^2_{\eta_{\rm I}\eta_{\rm I}}, \\ \sigma^2_{\Delta t_i \Delta\eta_j} &= \sigma^2_{\Delta\eta_i \Delta t_j} = \sigma^2_{t_{\rm I}\eta_{\rm I}}. \end{aligned} \tag{4.12}$$

We marginalize over (ι, ψ) using Eqs. 4.4 and 4.5:

$$\chi^2_\zeta(\theta,\phi) = -2\log\left(\frac{1}{f(\theta,\phi)} \int e^{-\chi^2_\zeta(\theta,\phi,\iota,\psi)/2}\, f(\theta,\phi,\iota,\psi)\, d\iota d\psi\right) \tag{4.13}$$

2. If variables are correlated, the variance of their sum is the sum of their covariances.

In addition to the timing and phase differences, the relative values of SNR received by each detector in the GW network also provides constraints on the source location. Different detectors are sensitive to different polarizations of the incoming waves, and the relative response in each detector depends upon the binary sky location (θ, ϕ) and orientation (ι, ψ), as well as the detector placement on the Earth, orientation of the detector arms, and the detector sensitivity, $S_h(f)$. The SNR measured in a given GW detector depends on the antenna response of the detector, as well as the binary source parameters, such as the luminosity distance, redshift, and chirp mass. Aside from chirp mass, these binary parameters are poorly constrained by the detection pipeline. However, since for our purposes we are only concerned with sky position, we can eliminate the other binary parameters by taking the ratio of the SNR measured at pairs of detectors. This ratio is solely a function of the detectors' antenna power patterns (Eq. 4.2) and sensitivities (Eq. 4.3):

$$\frac{\rho_i^2}{\rho_j^2}(\theta, \phi, \iota, \psi) = \frac{\Omega_i(\theta, \phi, \iota, \psi)\, I_{7,i}}{\Omega_j(\theta, \phi, \iota, \psi)\, I_{7,j}}.$$

We estimate the Gaussian uncertainty in SNR following the Fisher matrix calculation (Cutler & Flanagan, 1994):

$$\frac{\sigma_\rho}{\rho} = \frac{1}{\rho}, \tag{4.14}$$

which corresponds to a $\sim 10\%$ error in SNR measurement for a detection threshold of $\rho_{\rm th} \sim 12$. The *measured* SNR will be Gaussian distributed about the theoretical value $\tilde{\rho} = G(\rho, \sigma_\rho)$. Unlike the arrival time difference, the SNR ratio is not linear in SNR, so the error in the ratio is not described by a Gaussian. However, by taking the logarithm of the SNR ratio:

$$R_{ij}(\theta, \phi, \iota, \psi) \equiv \log \frac{\rho_i}{\rho_j} = \log \rho_i - \log \rho_j, \tag{4.15}$$

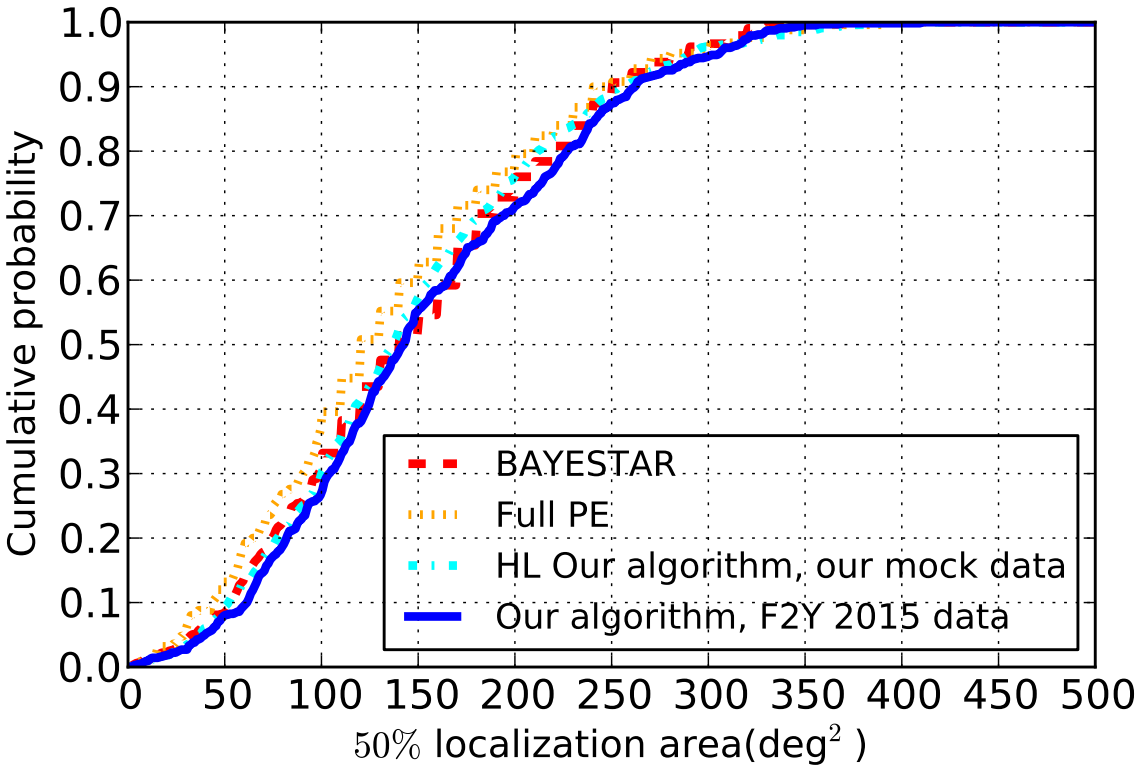

Figure 4.1: Cumulative 50% confidence localization areas of the 630 simulated sources taken from Singer et al. (2014) detected by LIGO Hanford+Livingston with the noise curve in LIGO-T1200307.

we find that the error in R approximates a Gaussian with variance [3]

$$\sigma^2_{R_{ij}} = \frac{1}{\rho_i^2} + \frac{1}{\rho_j^2}.$$

Similar to the case with arrival times, there are $N-1$ independent SNR ratios from a network consisting of N independent detectors. Therefore we define $R_i \equiv \log(\rho_I/\rho_i)$, $i \neq I$

3. The error becomes increasingly non-Gaussian when the SNR in one detector falls below ~ 5. This leads to a loss of the catch percentage at high confidence level, though this deviation is insignificant ($< 1\%$).

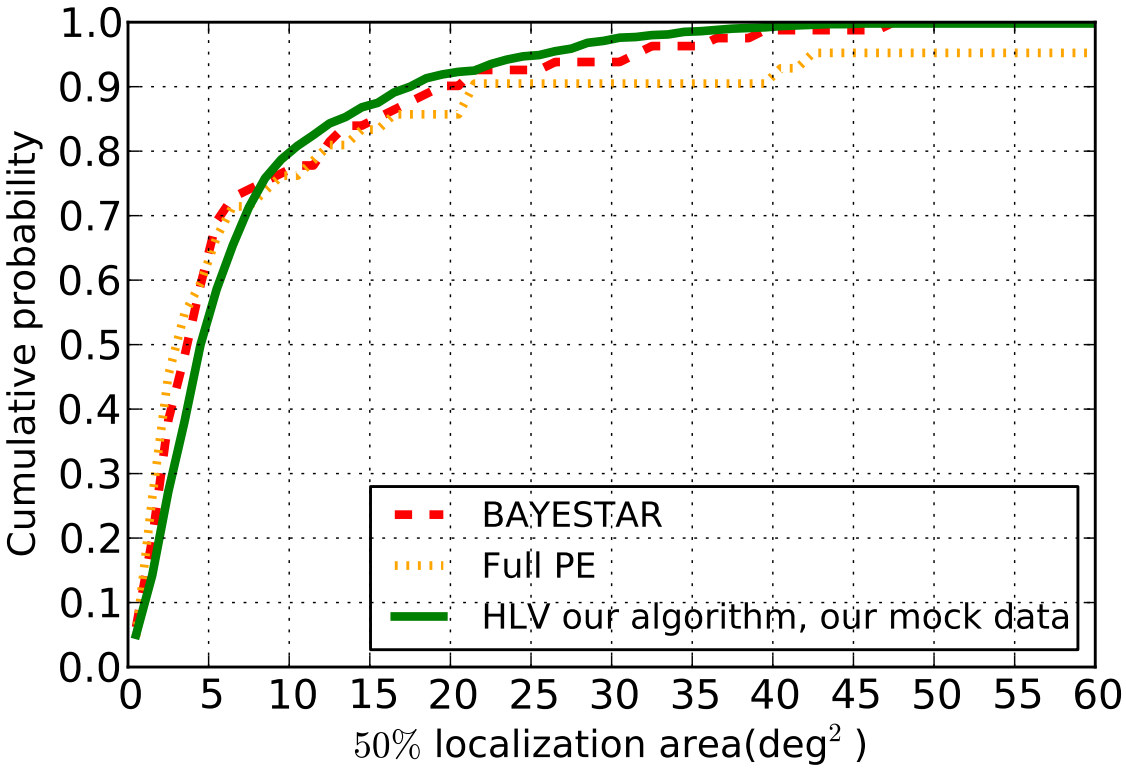

Figure 4.2: Cumulative 50% confidence localization areas of the 81 simulated sources taken from Singer et al. (2014) detected by LIGO Hanford+Livingston and Virgo with the noise curves in LIGO-T1200307 and Abbott et al. (2016a). We only consider events with SNR greater than 4 in all three detectors.

with an arbitrary reference detector I. The chi-square for SNR is then:

$$\chi^2_\rho(\theta,\phi,\iota,\psi) = \sum_{i,j}[\tilde{R}_i - R_i(\theta,\phi,\iota,\psi)]V^{-1}_{ij}[\tilde{R}_j - R_j(\theta,\phi,\iota,\psi)] \tag{4.16}$$

where $V_{ij} \equiv \mathrm{cov}(R_i, R_j)$ is the covariance matrix. If $i = j$ then

$$\sigma^2_{R_iR_i} = \frac{1}{\rho^2_I} + \frac{1}{\rho^2_i},$$

while if $i \neq j$ then we find:

$$\begin{aligned}
\sigma^2_{R_i R_j} &= \frac{1}{2}[\sigma^2_{R_i} + \sigma^2_{R_j} - \mathrm{var}(R_i - R_j)] \\
&= \frac{1}{2}(\sigma^2_{R_i} + \sigma^2_{R_j} - \sigma^2_{R_{ji}}) \\
&= \frac{1}{2}\left(\frac{1}{\rho_I^2} + \frac{1}{\rho_i^2} + \frac{1}{\rho_I^2} + \frac{1}{\rho_j^2} - \frac{1}{\rho_i^2} - \frac{1}{\rho_j^2}\right) \\
&= \frac{1}{\rho_I^2}.
\end{aligned} \tag{4.17}$$

By taking the logarithm of the power ratio (Eq. 4.15) we are able to estimate the covariance matrix analytically.

As shown in Eq. 4.16, the directional information is degenerate with binary inclination and orientation. We marginalize over (ι, ψ) using Eqs. 4.4 and 4.5:

$$\chi^2_\rho(\theta, \phi) = -2 \log \left(\frac{1}{f(\theta, \phi)} \int e^{-\chi^2_\rho(\theta, \phi, \iota, \psi)/2} \, f(\theta, \phi, \iota, \psi) \, d\iota d\psi \right). \tag{4.18}$$

To evaluate this equation we grid the binary inclination and orientation into 50 points each (2,500 points in total), calculate the integrand at each grid point, and then sum up the integrand. We assume that the noise curve is known and fixed, allowing pre-calculation of the I_7 term (Eq. 4.3). Changes in the noise curves can be captured by the detection pipeline, and incorporated into our algorithm. The ratio of I_7 terms, which is the relevant quantity since we are concerned with the ratio of SNR, is insensitive to changes in total mass for $M \lesssim 10\, M_\odot$. The sky prior (Eq. 4.4) also contributes to the posterior, so we define the total chi-square as: $\chi^2(\theta, \phi) \equiv \chi^2_{\vec{\epsilon}}(\theta, \phi) - 2 \log f(\theta, \phi)$. Eq.4.1 is then proportional to $e^{-\chi^2(\theta,\phi)/2}$. We grid the sky uniformly in $(\cos\theta, \phi)$ (or in (θ, ϕ) when close to the poles) [4], calculate χ^2 at each grid point, and then find the minimum χ^2_{min} from which to determine $\Delta\chi^2$ at each point and establish the posterior (Eq. 4.1). We use a contour defined by $\Delta\chi^2 = b_p$ to

4. We grid the sky uniformly in $(\cos\theta, \phi)$ with $d\cos\theta = d\phi = 0.005$ ($\sim$0.3 degree) for the two detector case. We use a finer gridding in the 3 detectors case, $d\cos\theta = d\phi = 0.0025$ ($\sim$0.14 degree)

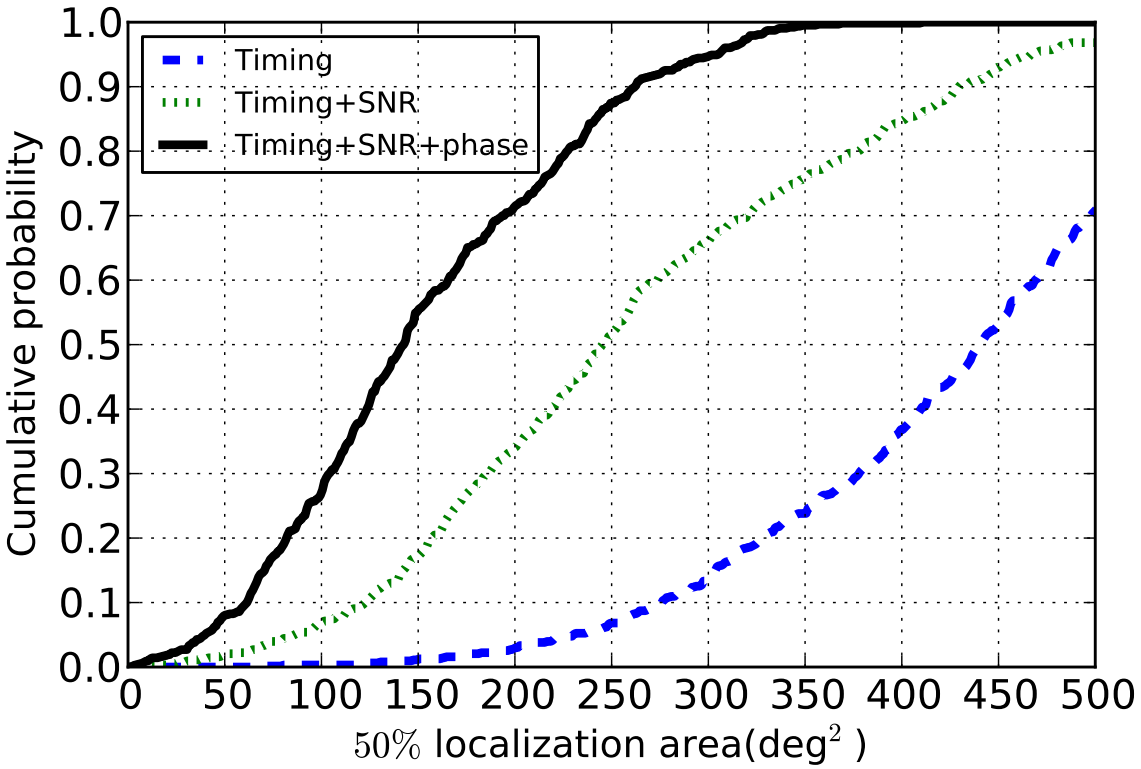

Figure 4.3: Comparison of the improvement in using time of arrival+SNR and time of arrival+SNR+phase. The simulated sources were taken from Singer et al. (2014) and localized with LIGO Hanford and Livingston.

determine the boundary of the localization area, such that

$$\frac{1}{n}\int_{\Delta\chi^2(\theta,\phi)<b_p} e^{-\Delta\chi^2(\theta,\phi)/2}\, d\theta d\phi = p\,\%, \tag{4.19}$$

where n normalizes the probability to 1. We vary the $\Delta\chi^2$ value of the boundary, b_p, until the integral in Eq. 4.19 reaches the desired confidence level $p\,\%$. If the posterior is Gaussian, we can calculate b_p analytically. The sky prior (Eq. 4.4) and the marginalization (Eq. 4.18) break the Gaussianity. However, we still use contours of constant $\Delta\chi^2$ as the boundaries of our confidence level, where we explicitly compute the probability incorporated within each contour rather than assuming the analytic value appropriate for true Gaussian

distributions (Press et al., 2007).

In summary, for a given event we use Eqs. 4.1, 4.6, and 4.19 to estimate the localization area on the sky. As a test, we apply our localization algorithm to the simulated source catalog from Singer et al. (2014), and compare our localization areas to those found from the BAYESTAR algorithm. As shown in Fig. 4.1, we find excellent consistency. We also explore the contribution to the localization determination arising from incorporating SNR and phase information in addition to timing, finding that the resulting localization areas decrease significantly (Fig. 4.3). In order to test our posterior, we determine the fraction of binaries which fall within our localization areas, and compare this to the predicted percentages. Fig. 4.4 shows that our formalism is self consistent. In order to further study the properties of our low-latency localization algorithm, we simulate a population of binary neutron stars. We follow the Monte Carlo approach we presented in Chen & Holz (2014) (see Chapter 3), utilizing the same noise curve as Singer et al. (2014). For each binary we calculate the true SNR and time-of-arrival in each detector. We then add in Gaussian noise for each of these quantities, mimicking the actual measurements (ignoring glitches; we have assumed a threshold SNR of $\rho_{\rm th} = 12$ to mimimize the importance of these). Our resulting distribution of localization areas is comparable to that in Figs. 4.1 and 4.2, indicating that our Monte Carlo sources and pipelines are consistent with that of Singer et al. (2014).

4.3 Loudest Event

As shown in Fig. 4.1 and 4.2, there is a broad distribution of localization areas for any given set of sources. This is related to the broad distribution of measured SNRs of the sources, which is in turn related to the distribution of distances to the sources. If not all GW triggers can be followed, the louder (higher SNR) events in general offer the opportunity for better localization and more efficient follow-up. In Fig. 4.5 we show the median localization area of the loudest source out of N events. The $N = 1$ case corresponds to the full distribution of

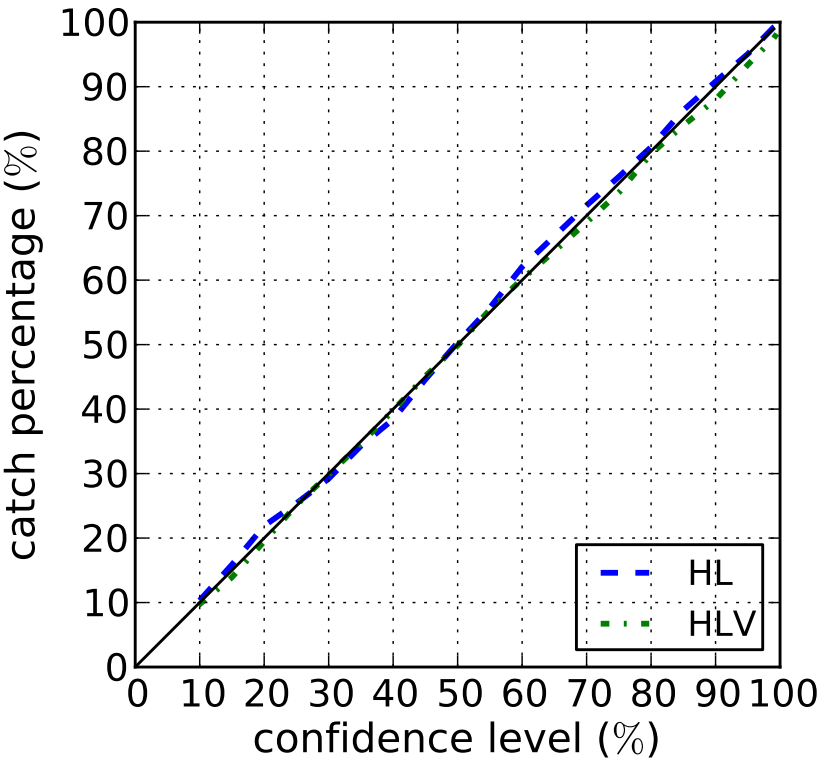

Figure 4.4: Integrated confidence level versus the actual captured percentage. The samples were taken from Singer et al. (2014) and localized with LIGO Hanford+Livingston (HL) and HL+Virgo (HLV). The black line is the $x = y$ line (perfect consistency). We find that the fraction of binaries found within our sky localization contours is in very good agreement with the predicted percentage.

localization areas for all events (also seen in Fig. 4.1). From Fisher matrix calculations the localization area is expected to scale as Area$\sim$ SNR^{-2}. This is true for 3 or more detectors, while for 2 detectors the sky locations are generally poorly constrained within a broad timing ring and the localization area will scale more slowly with improving SNR. In Chapter 3 we show that the distribution of detected SNRs follows a universal distribution. We also derive the universal loudest event distribution, which depends upon the detection threshold, $\rho_{\rm th}$,

and the number of events, N. The cumulative probability is:

$$F_{\rho_{\max}} = \left(1 - \left(\frac{\rho_{\rm th}}{\rho_{\max}}\right)^3\right)^N . \tag{4.20}$$

In Chapter 3 we pointed out that Eq. 4.20 is independent of the detector network, detector sensitivity, and all properties of the sources. Eq. 4.20 can applied to all situations (e.g. 2 or 3 detectors operating at different sensitivities looking for BNS, NS-BH, or supernovae), and we can predict the highest SNR out of N detections analytically. For example, the median of this distribution is given by:

$$\rho_{\max} = \frac{\rho_{\rm th}}{(1 - 0.5^{1/N})^{1/3}}.$$

If the localization area scales as Area$\sim$ SNR^{-2}, we would expect the ratio between the median area of the loudest out of N events, $A_{\max \rm N}$, and the median area of all events ($N = 1$), A_1, to scale as:

$$\frac{A_{\max \rm N}}{A_1} = \left(\frac{\rho_{\max \rm N}}{\rho_1}\right)^{-2} = \left(\frac{1 - 0.5^{1/N}}{0.5}\right)^{2/3} . \tag{4.21}$$

We fit for the area-SNR scaling index in Fig. 4.5. For 3 detectors we see that the area scales as SNR to the power of -2.04, while for the 2 detector case the scaling is shallower (-1.63) as expected.

Eq. 4.21 shows that the localization area shrinks rapidly as additional binaries are initially added: waiting for the loudest out of the first 4 events will reduce the expected sky area required for follow-up by a factor of 1.9 (2 detectors) and 2.2 (3 detectors). This improvement declines for larger sets of binaries; going from 4 to 10 binaries reduces the sky area by an additional factor of 1.6 (2 detectors) and 1.8 (3 detectors). This suggests that there may be an optimal strategy for selecting events for EM follow-up, based on the expected event rate

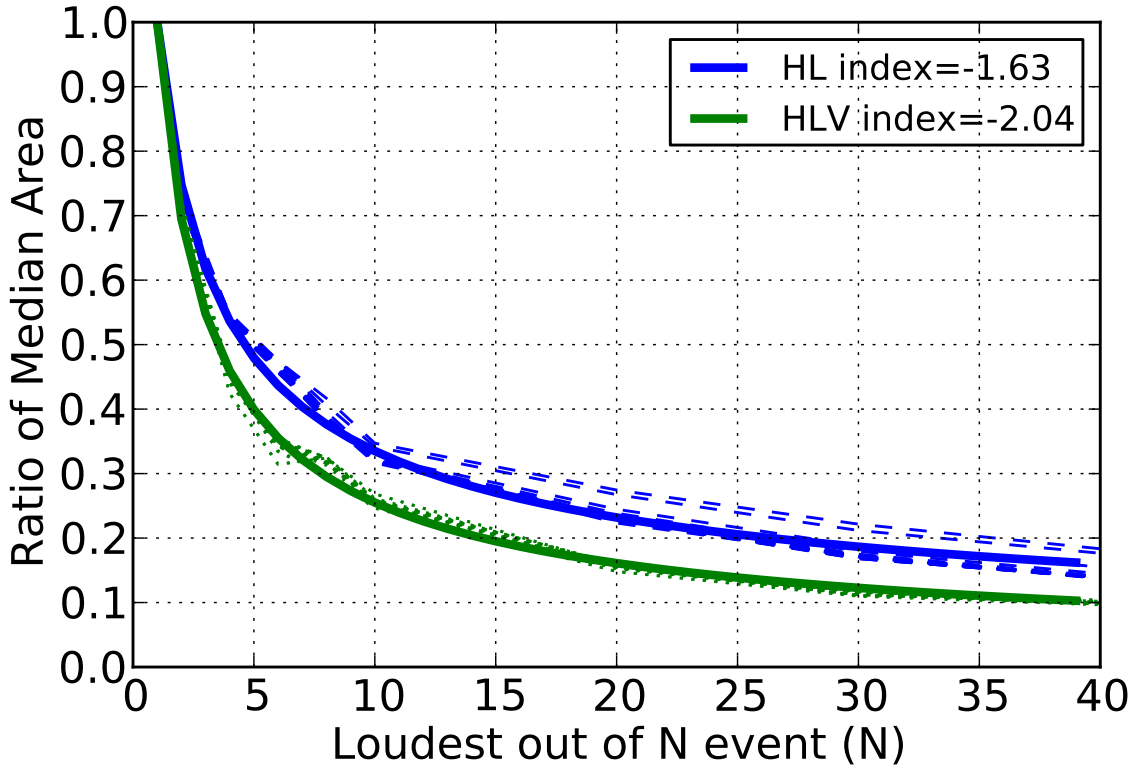

Figure 4.5: Ratio between the median localization area for the loudest event out of N detections and that for all events ($N = 1$). The SNR of the loudest events can be estimated from Eq. 4.20. For 3 detectors (HLV) the areas roughly scale as SNR^{-2} (index=-2.04), while for 2 detectors (HL) the scaling is shallower (index=-1.63).

and the observational constraints of the follow-up facility.

4.4 GRB Joint Localizations

Short GRBs are thought to be the very bright EM counterpart of binary neutron star or neutron star-black hole coalescence (Kocevski et al., 2010; Fong et al., 2013; Fong & Berger, 2013). If a short GRB is accompanied by GW emission, joint GW+EM detection would confirm the binary nature of the short GRB engine as well as help constrain the binary parameters. For example, the existence of gamma-ray emission would suggest that at least one of the members of the binary is a neutron star, and measurements of the inclination

would help constrain properties of the beamed jet. In addition, the shape and area of the localization of the GRB in gamma-rays is independent of the Advanced LIGO & Virgo localization, and thus combining the two localization areas can significantly constrain the sky position of the source.

We would like to explore the benefit to sky localization of a prior constraint on the inclination. Let us consider the case where a GRB has been observed, and we thereby have a prior on the GRB beaming angle which comes into Eqs. 4.4, 4.13, and 4.18. We randomly generate 3,000 binary neutron star mergers following the approach in Chapter 3. As suggested by observations, we assume that GRBs are beamed within the range 1–10° (Soderberg et al., 2006; Burrows et al., 2006; Coward et al., 2012; Fong et al., 2012), and we confine the orientation of our binaries to be uniformly distributed in $\cos\iota$ within $\pm\cos 1^\circ$, $\pm\cos 5^\circ$, $\pm\cos 10^\circ$ (3 samples of 1,000 binaries each). For each beaming angle distribution, we localize the source by marginalizing over the corresponding range of inclination angles ("$\sin\iota \leq \sin\theta_j$" which allows for both face-on and tail-on beaming; see Table 4.1) or over the full range of inclinations ("random ι"). We then compare the localization area and summarize the results in Table 4.1. Using the beaming prior only improves the localization by $< 10\%$, even in the case of 1° beaming. This is due to the unknown direction of rotation; a clockwise binary produces a different phase pattern than a counter-clockwise binary, and knowing that a binary is almost face-on *or* almost tail-on is not as useful as knowing that a binary is definitely one or the other. If we assume that we break the clockwise/counter clockwise degeneracy, the localization improves significantly, approaching the "known ι" case.

It is to be noted that additional measurements of phase, e.g., from Virgo, LIGO-India, or KAGRA, do not help to break this degeneracy. This is because a clockwise binary "above" a detector produces an identical waveform to a counter-clockwise binary "below". Alternatively, if the sky position is known, the GW network can determine whether the binary is orbiting clockwise or counter-clockwise.

θ_j	known ι	$\sin\iota \leq \sin\theta_j$	random ι
1°	340 deg^2	490 deg^2	540 deg^2
5°	340 deg^2	500 deg^2	530 deg^2
10°	350 deg^2	510 deg^2	530 deg^2
10°, clockwise	···	350 deg^2	···

Table 4.1: Hanford+Livingston median 90% localization area for binary neutron stars beamed within θ_j. The localizations are for three different sets of priors: knowing the exact inclination ("known ι"), knowing the beaming angle ("$\sin\iota \leq \sin\theta_j$") but not whether it is clockwise or counter-clockwise, and assuming no information about beaming ("random ι"). The last row corresponds to binaries that are beamed within 10° and revolve in the clockwise direction on the sky, and where the prior assumes not only the beaming but also the clockwise direction.

Although a beaming prior is of limited utility in determining position, the contribution of an independent localization from EM measurements of a GRB can be significant. The Fermi Gamma-ray Burst Monitor (GBM) telescope has a field-of-view of 8 steradians. It observes $\sim$ 45 short GRBs a year, potentially serving as a triggering system for binary mergers. A limitation of the Fermi GBM is that it can only localize sources within tens to hundreds of square degrees (Briggs et al., 2009). We conservatively assume that Fermi GBM localizes sources to a 100 deg^2 (1σ) 2D circular Gaussian. This independent likelihood function contributes to the posterior as an additional $\chi^2_{\rm Fermi}$. Fig. 4.6 shows the significant improvement in source localization which results from joint detections from Fermi and advanced GW detectors. The median of the 90% confidence ($\sim 2\sigma$) area for joint detection lies around 120 deg^2 even with only two GW detectors, as compared with 460 deg^2 and 560 deg^2 for the GRB and GW localizations, respectively. In this case the beaming priors make no difference whatsoever in the localization.

4.5 Discussion

We have developed a low latency localization algorithm for ground-based GW detector networks. Our approach requires the timing, phase, and SNR of the sources (provided by the

detection pipeline), and within a fraction of a second produces a 2D localization. We have implemented our algorithm for the case of non-spinning compact binary coalescences, assuming representative output from the detection pipeline (GSTLAL, Cannon et al. (2012)); this can in principle be generalized to other (preferably modeled) burst sources. Although the sky location is degenerate with other physical properties (e.g. masses, distances, and spins of the binaries), our algorithm avoids the need to estimate these parameters by instead utilizing the difference in arrival times, difference in phases, and the ratio of measured SNRs. This increases the simplicity and speed of localization, while reducing potential errors. Imprecise waveforms can result in errors in the SNR measurements, but the ratio of SNRs between detectors is less sensitive to these errors. By taking the SNR ratio, the parameter space is highly reduced.

For binary mergers, the two relevant unknowns are the binary orientation and inclination; it is computationally inexpensive to pre-calculate the marginalization of these over the entire sky. The timing and sky priors can also be pre-gridded and pre-calculated, simplifying the localization algorithm to a χ^2 determination using a look-up table combined with direct summation. Once the tables are loaded into memory, the entire algorithm takes < 1 second on a laptop (using a Python 2 script running on one thread on a 2.3 Ghz Intel Core i7). It would be straightforward to parallelize the algorithm (e.g., by having each core analyze a fraction of the sky), leading to sky localization within 0.1 seconds or better. There is ongoing work to speed up the detection pipeline (Chu et al., 2016), including the possibility of event detection before merger. This capability is only of use when coupled with rapid localization; our prompt and accurate algorithm offers the possibility of real-time localization contemporaneous with the inspiral and merger of the binary. It is to be noted that our algorithm can be generalized to calculate distance as well as sky position, allowing for the possibility of low-latency 3D localization.

In Fig. 4.2 we show the cumulative distribution of 50% localization areas for the first

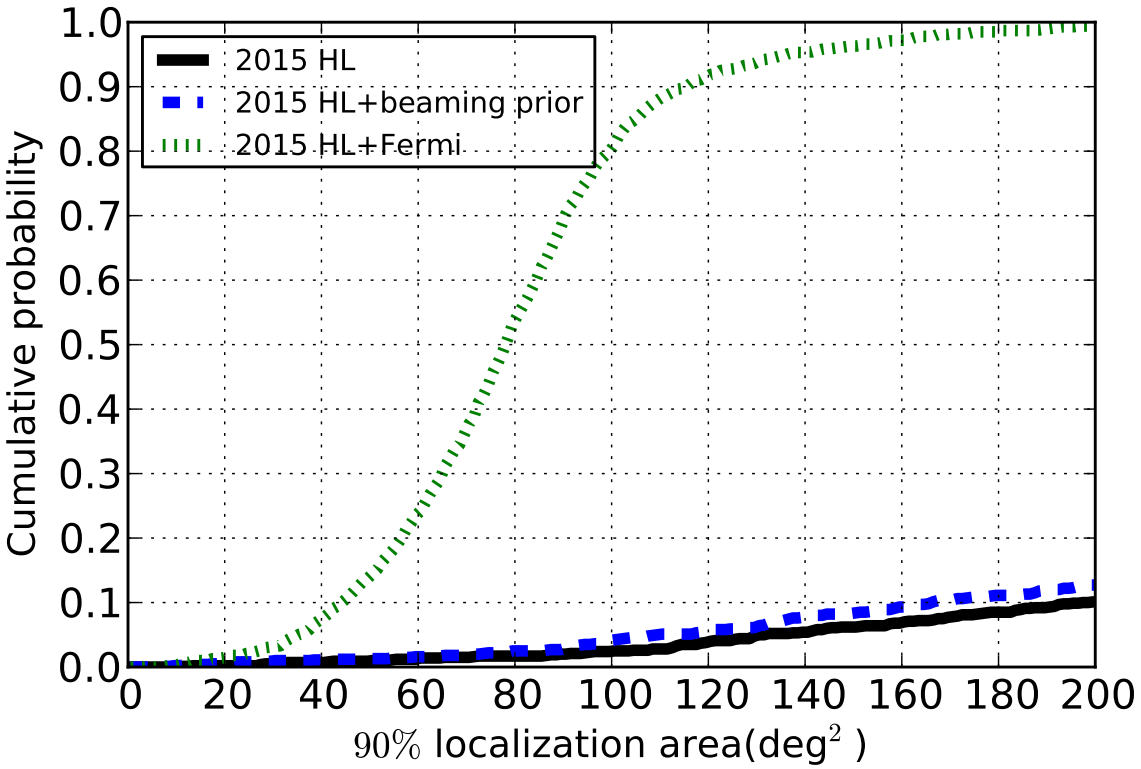

Figure 4.6: Cumulative distribution of sky localization for joint GW and Fermi GBM detections of short GRBs. This shows significant improvement, as compared with GW detection alone (Table 4.1).

two years of advanced LIGO and Virgo network operation. Although the localization is significantly improved with the addition of Virgo (c.f. Fig. 4.1), these represent a minority ($\sim 25\%$), since most events detected by this network have a Virgo SNR below the detection threshold ($\rho_{\rm V} < 4$) due to Virgo's lower sensitivity and mis-aligned antenna power pattern (Chen & Holz (2014) or see Chapter 3). Unless the detection pipeline produces information for these sub-threshold events, the low-latency localization will be based on information from only two detectors (i.e., H and L), followed by better localization resulting from the full parameter estimation pipeline analyzing the sub-threshold waveforms (Singer et al., 2014); we note that there is a potential remedy to this discussed in Section IX of Singer and Price (2015). For sources detected with only 2 detectors, the localization of events with the 2016

network is potentially worse than those detected in 2015 (Singer et al., 2014). This is because the effective bandwidth of the 2016 noise curve may be narrower than the 2015 case, leading to inferior localization for sources with the *same measured* SNRs (e.g., SNR=12). Of course, the 2016 network would detect sources from the 2015 network at higher SNR, and therefore would do a superior job of localizing identical sources. Occasionally the event will trigger only H+V or L+V. In these rare situations the localization will generally be worse than H+L, not only because Virgo operates at lower sensitivity, but also because the Virgo SNR distribution skews to lower values when coupled with an H or L detection (Chen & Holz (2014) or see Chapter 3).

We explore the dependence of localization on SNR, confirming that high SNR events lead to better localization. Since there is a universal distribution of SNR, we can use this to estimate the benefit of waiting for loud events. Fig. 4.5 shows that waiting for the loudest out of the first 4 events shrinks the median localization area by a factor of almost 2. For the first two GW detections (Abbott et al., 2016b; Abbott et al., 2016) there was a broad range of EM follow-up (Abbott et al., 2016c). Additional detections are to be expected in future LIGO-Virgo science runs (Abbott et al., 2016b,c; Belczynski et al., 2016b,a), and deciding which events to follow-up, given limited telescope resources, can be informed by our work. We provide the distribution of expected localization areas, which when tied to the expected number of detections can be used to inform the triggering of follow-up observations. Our work has beeen implemented in the Dark Energy Camera follow-up of the first two GW detections (Cowperthwaite et al., 2016; Soares-Santos et al., 2016), and can be applied to other follow-up programs with limited telescope resources.

Fig. 4.6 shows that combining an EM prior on the sky location of a source with GW localization greatly improves the resulting localization. This is because the shapes of the two localization regions are ver different and completely uncorrelated. Fermi GBM detection of a short GRB would then greatly enhance the localization resulting from a GW network. One

might have thought that such a detection would also place useful prior constraints on the beaming angle (i.e., gamma-ray detection implies that the binary is face-on). However, Table 4.1 and Fig. 4.6 demonstrate that the beaming prior makes only a marginal improvement in localization because of the degeneracy between face-on and tail-on binaries.

We have developed a simple, fast, and accurate algorithm for the localization of GW sources. This algorithm, when coupled with a fast detection pipeline, can play an important role in the development of multi-messenger astronomy.

We acknowledge valuable discussions with Leo Singer, Larry Price, Ben Farr, and Tyson Bailey Littenberg.

CHAPTER 5

FINDING THE ONE: IDENTIFYING THE HOST GALAXIES OF GRAVITATIONAL-WAVE SOURCES

5.1 Introduction

The era of gravitational-wave astrophysics has arrived (Abbott et al., 2016; Abbott et al., 2016b), and we now await multi-messenger astronomy to achieve the full scientific potential of these detections. The observation of an electromagnetic [1] (EM) counterpart to a gravitational-wave (GW) source would allow us to more fully characterize and understand the physics and astrophysics of the sources. In addition to direct EM counterparts to the GW events, there is also enormous interest in identifying the host galaxies to these events. For example, measurements of the stellar age, mass, or metallicity of host galaxies, perhaps even as a function of redshift or binary total mass, could lead to major insights and constraints regarding astrophysical formation mechanisms (Abbott et al., 2016a). Furthermore, host galaxies will provide independent estimates of redshift, allowing for the use of gravitational-wave sources as standard sirens (Schutz, 1986; Dalal et al., 2006). Finally, by identifying a host galaxy we dramatically increase the probability of identifying a transient counterpart associated with the event, since we are then able to utilize sensitive narrow-field instruments to search for the counterpart and we reduce the likelihood of contamination.

There are two generic ways to identify the host galaxy of a GW event. The first is by detecting a transient counterpart that can be directly associated with the gravitational-wave event. Once the transient is detected, one can often directly identify the host galaxy. This approach has generated enormous interest, spawning a very active EM follow-up community (Abbott et al., 2016c; Soares-Santos et al., 2016; Annis et al., 2016; Cowperthwaite et al., 2016).

1. Under "electromagnetic" we also include particle messengers, such as neutrinos and cosmic rays.

An alternate way to identify a host is by examining the three-dimensional localization volume associated with the GW event. As originally noted by Schutz (1986) and later expanded by Del Pozzo (2012), this approach can be used in a statistical fashion: although any individual GW event may have many potential host galaxies within the relevant localization volume, by analyzing many events simultaneously, statistical properties of the host galaxies (such as their redshifts) can be inferred. An essential aspect of this approach is the size of the localization volume: the smaller the volume, the smaller the number of potential host galaxies contained within, and the easier the statistical task of identifying the true host. Previous work has indicated that these volumes are $> 10^4\,\mathrm{Mpc}^3$, corresponding to >hundreds of potential galaxies (Nissanke et al., 2013b; Hanna et al., 2014; Gehrels et al., 2016; Singer et al., 2016a,b).

We re-examine the localization volumes associated with sources identified by ground-based gravitational-wave detector networks. We perform a systematic study, incorporating a range of networks and a range of potential sources, and simulate tens of thousands of GW detections. This study is enabled by our rapid GW sky localization algorithm (Chen & Holz (2015) or see Chapter 4), which we have extended to produce low-latency 3D volume localizations. We focus on the loudest events, exploiting the fact that the distribution of detected signal-to-noise ratios is universal (Chen & Holz (2014) or see Chapter 3) and that loud events can be anticipated and are inevitable, and these events are generally well-localized (Chen & Holz (2015) or see Chapter 4). We find that the best localized events, which we call "golden" events [2], can be constrained to very small volumes, potentially containing only a single galaxy. For these golden events, the unique host galaxy may be identified, allowing for a direct EM association with the GW source.

2. Similar but not identical to the events discussed in Hughes & Menou (2005), which considered high SNR events for LISA as powerful tests of strong-field general relativity.

5.2 Methods

We take a Monte Carlo approach, generating a large sample of binary coalescences throughout the Universe and then investigating the fraction which can be detected by various GW networks, and producing the distributions of localizations associated with these detections. We generate $1.4M_{\odot}$–$1.4M_{\odot}$, $10M_{\odot}$–$10M_{\odot}$, and $30M_{\odot}$–$30M_{\odot}$ binary mergers at random sky positions with random inclinations and orientations. The waveforms of these mergers were generated using the waveform generator in LALSuite (https://wiki.ligo.org/DASWG/LALSuite). For the $1.4M_{\odot}$–$1.4M_{\odot}$ binaries we use the TaylorF2 waveform (Yunes et al., 2009), and for the $10M_{\odot}$–$10M_{\odot}$ and $30M_{\odot}$–$30M_{\odot}$ binaries we use the IMRPhenomD waveform (Khan et al., 2016). We assume aligned spin and ignore precession; including general spins should not qualitatively change our results, and in general would lead to slightly improved localization (Farr et al., 2016). We consider two GW detector network configurations ('HLV' and 'HLVJI') [3] at two different sensitivities ('O3' and 'design'). The 'O3' sensitivity for H and L corresponds to a binary neutron star (BNS) range [4] of 120 Mpc, while for V the range is 60 Mpc (Abbott et al., 2016a). The 'design' sensitivity for all detectors is taken from the "aLIGO" curve in LIGO Document T1500293 (https://dcc.ligo.org/LIGO-T0900288/public), corresponding to a BNS range of 200 Mpc. Using these waveforms and detector sensitivities we calculate the optimal matched filter signal-to-noise ratio (SNR), ρ, at each detector:

$$\rho = \left(\int \frac{|\tilde{h}(f)|^2}{S_h(f)}\, df \right)^{1/2}, \tag{5.1}$$

where $\tilde{h}(f)$ is the Fourier transform of the waveform in the frequency domain and $S_h(f)$ is the detector power spectral density. We add Gaussian noise of width 1 to the SNR, and calculate the network SNR as the root-sum-square of the noise-added individual detector

3. H: LIGO-Hanford, L: LIGO-Livingston, V: Virgo, J: KAGRA, and I: LIGO-India

4. The range is defined as the average luminosity distance to events detected by a single detector with signal-to-noise ratios greater than 8.

SNRs. Our detection threshold requires that the network SNR be greater than 12. For detectable events we calculate the time-of-arrival difference and phase difference between pairs of detectors, and add in Gaussian errors following the Fisher matrix formalism (Cutler & Flanagan, 1994). The cumulative distribution of the luminosity distance of the detected events is shown in Fig. 5.1; note the tails to nearby events for all scenarios.

In order to localize the source we follow a similar approach to our previous work in Chapter 4. We use the measured difference in arrival time, the measured difference in phase, and the measured SNR in the individual detectors to reconstruct the 3D location of the source. In our simulations the binary mergers are distributed uniformly in comoving volume and the cosmological parameters are taken to be ($\Omega_m = 0.308, \Omega_\Lambda = 0.692, h = 0.678$) (Planck Collaboration et al., 2016). Our Bayesian prior assumes the same cosmological parameters, and is also uniform in comoving volume. To calculate the posterior, we grid the sky using healpix pixels (http://healpix.jpl.nasa.gov) and 100 bins in luminosity distance. We scale the resolution in sky direction and luminosity distance depending on the measured SNR of the events, with higher SNR events having finer resolution (e.g., 3.3×10^{-3} deg^2 sky pixels for network SNR of 110). For each binary above the network detection threshold we produce a joint likelihood in sky position and distance. For each voxel (3D volume pixel) we produce a probability. We then rank order the probabilities, and starting with the highest probability voxel we sum until we have reached the desired probability threshold. In this manner we produce the 90% likelihood volumes. We take the 3D likelihood and project it to obtain the 2D sky localization. Similarly, we then rank the 2D pixels to produce the 90% likelihood localization areas.

5.3 Results

Our results are summarized in Fig. 5.2 and Tables 5.1 and 5.2. Fig. 5.2 shows a plot of the cumulative distribution of the 90% localization volumes. We find that 50% of the BNS

sources will be localized to a volume of $\sim 10^4\,\mathrm{Mpc}^3$, regardless of detector network.

We are particularly interested in the number of galaxies that can be expected in the localization volumes. To estimate this, we assume that the number density of galaxies is $0.01/\mathrm{Mpc}^3$. This estimate takes the Schechter function (Schechter, 1976), with B-band parameters $\phi_* = 1.6\times10^{-2}h^3\,\mathrm{Mpc}^{-3}$, α=-1.07, $L_* = 1.2\times10^{10}h^{-2}L_{B,\odot}$, and $h = 0.7$ (where $L_{B,\odot}$ is the solar luminosity in B-band), and integrate down to $0.12\,L^*$ corresponding to 86% of the total luminosity (Norberg et al., 2002; Liske et al., 2003; González et al., 2006; Gehrels et al., 2016).

The top axis in Fig. 5.2 shows the expected number of galaxies in the 90% localization volumes. For example, a localization volume of 1,000 Mpc^3 corresponds to an expectation of 10 galaxies, while a localization smaller than 100 Mpc^3 corresponds to on average a single galaxy within the localization volume. In other words, for GW sources localized to within 100 Mpc^3, it may be possible to directly identify the unique host galaxy without the need for an associated EM transient.

We have argued that a small fraction of GW sources are sufficiently well localized to allow for improved constraints on their host galaxies. But how many of these systems will actually be detected? To estimate this we need to know the expected number of systems that will be detected by the various networks. With only a few systems detected to date, the rate of binary coalescences remains uncertain; we assume the rate for (1.4, 1.4), (10, 10), and (30, 30) $M_\odot$ binary mergers to be [low, mean, high]: $[10^{-8}, 10^{-6}, 10^{-5}]$, $[1\times10^{-8}, 5\times10^{-8}, 2\times10^{-7}]$, and $[6\times10^{-9}, 2\times10^{-8}, 6\times10^{-8}]$ $\mathrm{Mpc}^{-3}\mathrm{yr}^{-1}$, respectively (Abadie et al., 2010; Abbott et al., 2016c,b,d). From these rates we are able to estimate the number of systems that will be detected with each GW network, and then use the results in Fig. 5.2 to infer the number of systems that will be localized sufficiently to identify the unique host galaxy. We summarize our results in Tables 5.1 and 5.2.

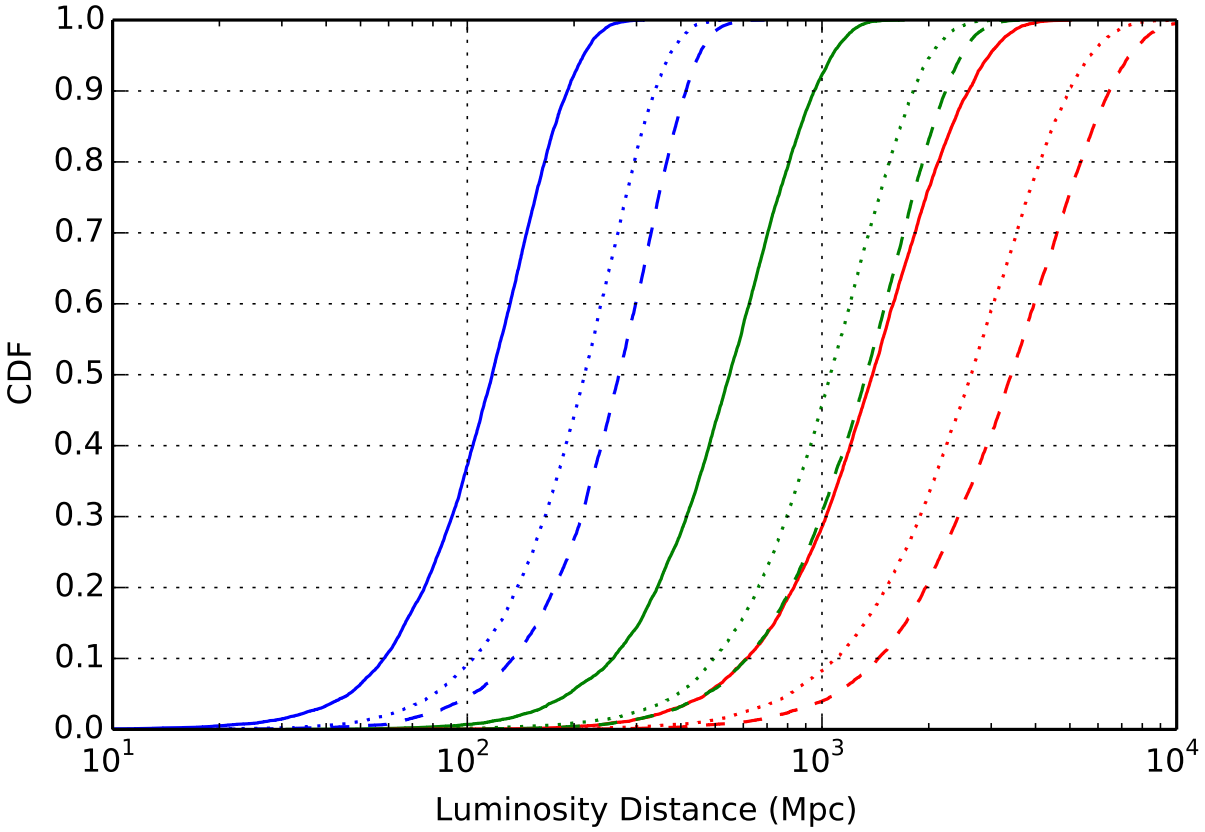

Figure 5.1: Cumulative distribution of the luminosity distances for the binary mergers detected in our simulated population. The categories of binary are $1.4M_\odot$–$1.4M_\odot$ (blue), $10M_\odot$–$10M_\odot$ (green), and $30M_\odot$–$30M_\odot$ (red). We consider three GW detector network configurations at different sensitivities: Solid–HLV at O3 sensitivity, dotted–HLV at design sensitivity, and dashed–HLVJI at design sensitivity. There are 10,000 simulated detectable/localized events for each type of binary systems and network configurations.

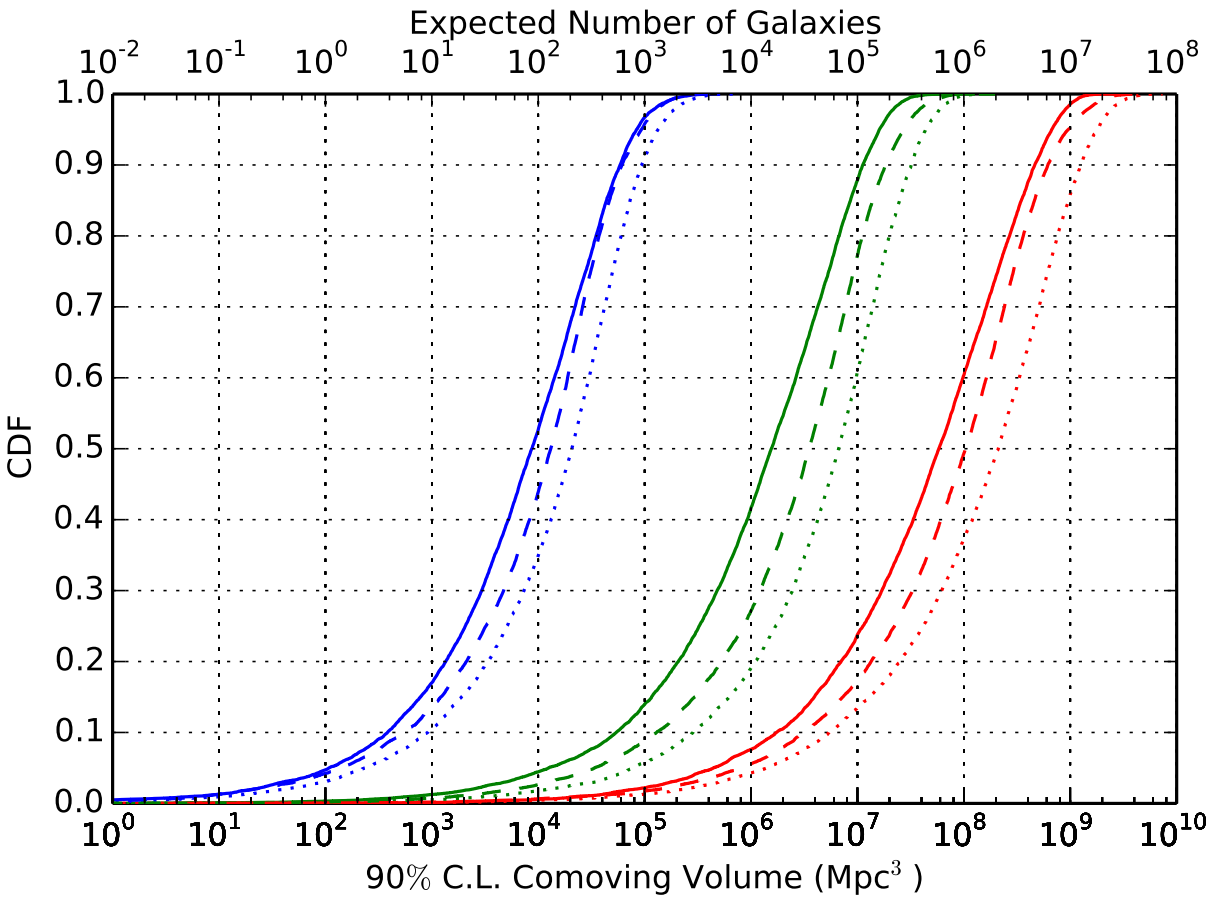

Figure 5.2: Cumulative distribution of the 90% confidence level localization comoving volumes for 10,000 simulated $1.4M_{\odot}$–$1.4M_{\odot}$ (blue), $10M_{\odot}$–$10M_{\odot}$ (green), and $30M_{\odot}$–$30M_{\odot}$ (red) binary mergers. We consider three GW detector network configurations at different sensitivities: Solid–HLV at O3 sensitivity, dotted–HLV at design sensitivity, and dashed–HLVJI at design sensitivity. The top axis shows the expected number of galaxies within the volume assuming a number density of galaxies of $0.01/\mathrm{Mpc}^3$ (see text).

Network	Mass($M_\odot$)	Median (Mpc^3)	<100 Mpc^3 (%)	<100 Mpc^3 ($\langle N_{\rm event}\rangle$)	<1000 Mpc^3 (%)	<1000 Mpc^3 ($\langle N_{\rm event}\rangle$)
HLV O3	(1.4, 1.4)	8.7×10^3	4.72	[0.0 , 0.24 , 2.37]	16.99	[0.01 , 0.85 , 8.55]
HLV O3	(10, 10)	1.6×10^6	0.32	[0.01 , 0.07 , 0.26]	1.25	[0.05 , 0.25 , 1.02]
HLV O3	(30, 30)	5.8×10^7	0.05	[0.01 , 0.04 , 0.12]	0.12	[0.03 , 0.1 , 0.3]
HLV design	(1.4, 1.4)	2.1×10^4	3.09	[0.01 , 1.27 , 12.69]	10.4	[0.04 , 4.27 , 42.66]
HLV design	(10, 10)	6.7×10^6	0.2	[0.06 , 0.31 , 1.22]	0.52	[0.16 , 0.79 , 3.17]
HLV design	(30, 30)	2.1×10^8	0.03	[0.05 , 0.15 , 0.46]	0.1	[0.15 , 0.51 , 1.53]
HLVJI design	(1.4, 1.4)	1.3×10^4	4.23	[0.04 , 3.53 , 35.3]	13.61	[0.11 , 11.36 , 113.56]
HLVJI design	(10, 10)	3.5×10^6	0.22	[0.13 , 0.65 , 2.58]	0.73	[0.43 , 2.14 , 8.56]
HLVJI design	(30, 30)	1.0×10^8	0.06	[0.16 , 0.55 , 1.65]	0.17	[0.47 , 1.56 , 4.67]

Table 5.1: 90% confidence level 3D localization comoving volumes. First column: detector network and sensitivity. Second column: mass of the binaries. Third column: median 90% confidence level localization volume. Fourth & sixth columns: fraction of events localized within 100 and 1,000 Mpc^3. Fifth & seventh columns: expected number of events localized within 100 and 1,000 Mpc^3 for [low, mean, high] event rate densities (see text for details). The run duration for O3 and design are taken to be 9 months and 1 year, with a duty cycle taken to be 100%.

There are a number of interesting aspects of our results:

- The localization volumes and sky areas are larger for more massive binaries. Massive binaries merge at lower frequency, and are generally detected to higher distances (see Fig. 5.1), and due to redshifting these binaries spend shorter time in the GW detectable band leading to a larger error in estimates of the time-of-arrival. For example, the median 10–10$M_\odot$ binary black hole localization area is ~ 2.5 times that of BNS systems at HLV O3 sensitivity, and this ratio increases to ~ 5 at design sensitivity as the binaries are detected farther away. Since the distance uncertainties are fractional, farther distances also correspond to larger volumes. We find that BNS systems are the most likely to be well localized, and therefore are the most likely to allow for unique host galaxy associations.

- The localization areas are smaller for improved gravitational-wave networks. This is because the localization is primarily dependent on the timing measurements at each detector, and as the networks improve the relative timing improves. Going from three detectors to five detectors causes a large improvement in the 2D localization.

- In all cases there is a tail to very well localized events, corresponding to events that are particularly loud and are fortuitously oriented and well located on the sky. For example, for BNS events localized within 1,000 Mpc^3 by the HLV network at design sensitivity, the average measured network SNR is 38.

- We find that $\sim 17\%$ of BNS sources detected with the HLV network in O3 will be localized to within $1{,}000\,\mathrm{Mpc}^3$, corresponding to < 10 galaxies within the 90% localization volume. One in 20 sources will be localized to within $100\,\mathrm{Mpc}^3$, potentially allowing for the identification of a unique host galaxy. These values become 3%/10% (at $100/1{,}000\,\mathrm{Mpc}^3$) for HLV at design sensitivity, and 4%/14% at HLVJI at design sensitivity.

- We find that a large fraction of BNS systems are 2D localized to better than 10 deg^2 for all network configurations; for HLVJI over 90% of sources are localized this well, with almost 10% localized to within 1 deg^2. The population of well-localized 2D systems overlaps significantly with the population of well-localized 3D systems; these are the high-SNR tail of the universal distribution (Chen & Holz (2014) or see Chapter 3).

- As the networks improve the fraction of well-localized events drops as increasing numbers of sources are detected at increasing distance. However, the total number of golden events will increase, since a golden event for a given network will only become "more golden" when detected by an improved network.

- We find that for all network configurations there is an expectation of ~ 1 golden event per year: a binary localized to a sufficiently small volume that a unique galaxy host may be identified.

Network	Mass($M_\odot$)	Median (deg^2)	$< 1\ \mathrm{deg}^2$ (%)	$< 1\ \mathrm{deg}^2$ ($\langle N_{\mathrm{event}} \rangle$)	$< 10\ \mathrm{deg}^2$ (%)	$< 10\ \mathrm{deg}^2$ ($\langle N_{\mathrm{event}} \rangle$)
HLV O3	(1.4, 1.4)	2.3×10^1	0.67	[0.0 , 0.03 , 0.34]	20.39	[0.01 , 1.03 , 10.26]
HLV O3	(10, 10)	5.9×10^1	0.23	[0.01 , 0.05 , 0.19]	7.45	[0.3 , 1.52 , 6.07]
HLV O3	(30, 30)	2.4×10^2	0.04	[0.01 , 0.03 , 0.1]	1.55	[0.38 , 1.28 , 3.83]
HLV design	(1.4, 1.4)	9.0×10^0	2.3	[0.01 , 0.94 , 9.42]	54.7	[0.22 , 22.44 , 224.39]
HLV design	(10, 10)	4.6×10^1	0.27	[0.08 , 0.41 , 1.65]	7.61	[2.33 , 11.64 , 46.56]
HLV design	(30, 30)	2.1×10^2	0.02	[0.03 , 0.1 , 0.31]	2.12	[3.25 , 10.83 , 32.49]
HLVJI design	(1.4, 1.4)	3.4×10^0	9.52	[0.08 , 7.94 , 79.42]	93.55	[0.78 , 78.07 , 780.67]
HLVJI design	(10, 10)	1.5×10^1	1.26	[0.74 , 3.7 , 14.78]	30.75	[18.08 , 90.38 , 361.54]
HLVJI design	(30, 30)	6.4×10^1	0.36	[0.99 , 3.3 , 9.89]	6.82	[18.79 , 62.62 , 187.87]

Table 5.2: 90% confidence level 2D localization areas. First column: detector network and sensitivity. Second column: mass of the binaries. Third column: median 90% confidence level localization area. Fourth & sixth columns: fraction of events localized within 1 and 10 deg^2. Fifth & seventh columns: expected number of events localized within 1 and 10 deg^2 for [low, mean, high] event rate densities.

5.4 Discussion

We have explored the ability of gravitational-wave detector networks to localize sources both on the sky and in space (sky localization + distance). We have derived the distribution of expected localizations for a range of detector networks and a range of sources. Of particular interest are the cases where the expected number of galaxies is $\langle N \rangle = 1$, since in these cases it is theoretically possible to identify the *unique* host galaxy associated with a GW source. We show that in all network configurations there exists a small percentage of sources that will be sufficiently localized so that only a single galaxy may be present in the localization volume. We find that even in O3 there is the likelihood of an event sufficiently well localized such that only a few galaxies will be found within its localization volume, and in the advanced detector era we expect tens of sources per year localized to only a very small number of potential host galaxies, and to be able to uniquely identify the host galaxy ~ 1 source per year. Fig. 5.2 show that localizations deteriorate quickly beyond the first few golden events, suggesting that the utility of this small sample of events may outweigh the rest of the population.

We now highlight a number of caveats to our results. We have ignored the role of systematic errors in the GW measurements. For example, a 5% systematic error in the distance estimates will lead to a 5% shift in the 90% confidence volume, and therefore potentially the wrong associated host galaxies. We have performed preliminary tests to show that, given the large spread in distance uncertainties, these effects remain sub-dominant at the 5% level. We have ignored gravitational lensing, since the best localized sources are generally the closest ones. For example, even for the 30–30 $M_\odot$ case, the maximum luminosity distance of our sample of binaries localized to within 1,000 Mpc^3 is $\sim$250 Mpc. This corresponds to a redshift of $\sim$0.055; gravitational lensing is expected to be negligible at this distance (Holz & Linder, 2005). We note that GW detectors localize sources in luminosity distance, while galaxies generically live in redshift space. In the work above we have assumed a given cosmology to perform this mapping. Since one of our goals is to use these

systems as standard sirens to measure cosmological parameters, one may be concerned that our cosmological assumptions preclude independent cosmological measurements. However, if we conservatively assume that the cosmological parameters are known to within 10%, it may nonetheless be possible to narrow down the number of host galaxies. These can then be used in turn to further constrain the cosmological parameters to better than 10% through the use of standard sirens. We have tested this explicitly. In addition, we have ignored the effects of galaxy clustering. For example, some volumes may center on clusters with a galaxy density orders of magnitude higher than the average. In these cases, identifying the individual host galaxy may become more challenging, although estimating the redshift of the cluster may nonetheless be possible.

Another important complication is the absence of complete galaxy catalogs within the localization volumes of interest. However, we have shown that the associated 2D sky localizations are small for events with well-localized volumes. For example, for BNS events localized by the HLV network at design sensitivity with $\langle N \rangle \sim 10$ galaxies within their localization volume, the median 90% sky localization area is 2.7 deg^2. Given that binaries are generally expected to be close to their host galaxies (within ∼arcmin for the golden binaries discussed here (Belczynski et al., 2006; Fong & Berger, 2013)), large-field survey telescopes such as the Dark Energy Camera (DECam), Hyper Suprime-Cam, and LSST would be able to fully cover these fields in a small number of pointings. Furthermore, as mentioned above, these well localized systems are the closest ones in the population, and therefore are expected to have correspondingly brighter host galaxies. For the maximum distance of the 30–30 $M_\odot$ case discussed above (250 Mpc), the B-band magnitude of a Milky Way-like galaxy would be ~ 16.6. Thus an instrument such as DECam would be able to build a complete galaxy catalog *in real time* across the entire localization region in a few short (~ 1 minute) pointings. In addition to building an on-the-fly galaxy catalog, the small number of potential host galaxies within the volume coupled with the comparatively nearby distances for these

well-localized sources will enable unparalleled triggered searches for EM counterparts. This is further enabled because our 3D localization algorithm presented in this letter, as well as other rapid localization algorithm such as BAYESTAR (Singer et al., 2016a), can be run in low latency ($\sim$ minutes).

Of particular interest is how these better-localized binaries will impact attempts to measure the Hubble constant with gravitational-wave standard sirens. In this case identifying a host galaxy is equivalent to identifying an EM counterpart since it allows for an independent measurement of the redshift. Although only a small fraction of the sources will be well-localized, since these directly allow for points on the Hubble diagram they provide uniquely powerful constraints (Dalal et al., 2006; Nissanke et al., 2010).

In conclusion, we have shown that there will exist a class of events which will be sufficiently well localized to allow us to narrow the potential number of host galaxies to a small number, and in extreme cases allow for the unique identification of the host of the GW source. These special cases will directly engender multi-messenger astronomy without the need for associated transient EM counterparts. These golden events are likely to be of particular interest in the development of GW astrophysics and cosmology.

We acknowledge Krzysztof Belczynski, Thomas Dent, Benjamin Farr, Will Farr, Christopher Messenger, John Miller, Salvatore Vitale, and Risa Wechsler for valuable discussions and comments.

CHAPTER 6

OBSERVATIONAL SELECTION EFFECTS WITH GROUND-BASED GRAVITATIONAL WAVE DETECTORS

6.1 Introduction

During the last years of initial LIGO and Virgo, as well as in advanced LIGO's first observing run (O1; Abbott et al., 2016b), a large consortium of electromagnetic (EM) observers were involved in following-up GW candidates (Abbott et al., 2016c; Aasi et al., 2014; Abadie et al., 2012a), and there has been substantial effort to plan and optimize EM follow-up. Previous work compared the advantages and disadvantages of different telescopes (Kasliwal & Nissanke, 2014). Regardless of a facility's hardware, observatories at different locations will have systematically different opportunities to follow up GW events due to properties of the GW detector network.

Even if astrophysical sources are distributed isotropically on the sky, GW detections with the two LIGO detectors will not be. Because of the detectors' locations (Hanford, WA and Livingston, LA) and duty cycles, detectable GW sources preferentially come from certain locations on the celestial sphere, and the preferred regions vary with the seasons. Follow-up of EM counterparts with emission timescales of less than a few weeks will be especially affected by these biases. In particular, the Earth's rotation limits ground-based EM follow-up facilities. Different sites can access different parts of the GW localization maps at different times and therefore have different expectations for the fraction of counterparts they can detect. These GW selection effects have other important ramifications for follow-up efforts, such as the amount of time before an average source will be accessible and the average air mass expected.

GW detectors do not operate continuously (Aasi et al., 2015; Abbott et al., 2016). Previous studies considered their duty cycle when estimating detection rates (Singer et al., 2014;

Abbott et al., 2016a,c). However, their operation is not uniformly distributed in time, and instead shows a strong preference for acquiring data during their local night. We describe this behavior quantitatively and assess its influence on GW detections as well as EM follow-up.

We first explain the sources of biases and their impact on GW detections in § 6.2. We show the effects of the bias on ground-based EM follow-up facilities in § 6.3, and conclude in § 6.4.

6.2 Observational bias introduced by ground-based gravitational wave detectors

Ground-based GW interferometers do not have isotropic sensitivity. Over time, the antenna pattern produces systematic preferences for the locations of detectable sources. These can be split into a dependence on the source's declination, which will not improve until additional detectors are added to the network, and a dependence on the source's right ascension, which can be mitigated with existing facilities.

6.2.1 Dependence on Declination

Because of projection effects, GW detectors are most sensitive to signals coming from above or below the plane defined by their arms (Thorne, 1987b). The two LIGO detectors, for example, are most sensitive, and equally sensitive, to sources directly above North America and above the Indian Ocean (Fig 6.1a). As the Earth rotates, the antenna pattern is swept across the celestial sphere, creating preferred bands in the mid-latitudes of both hemispheres (Fig 6.1b). This is determined primarily by the detectors' relative sensitivity and the geometry of the network. For the two LIGO detectors, we expect more detections at mid-declinations compared to low- or high-declinations.

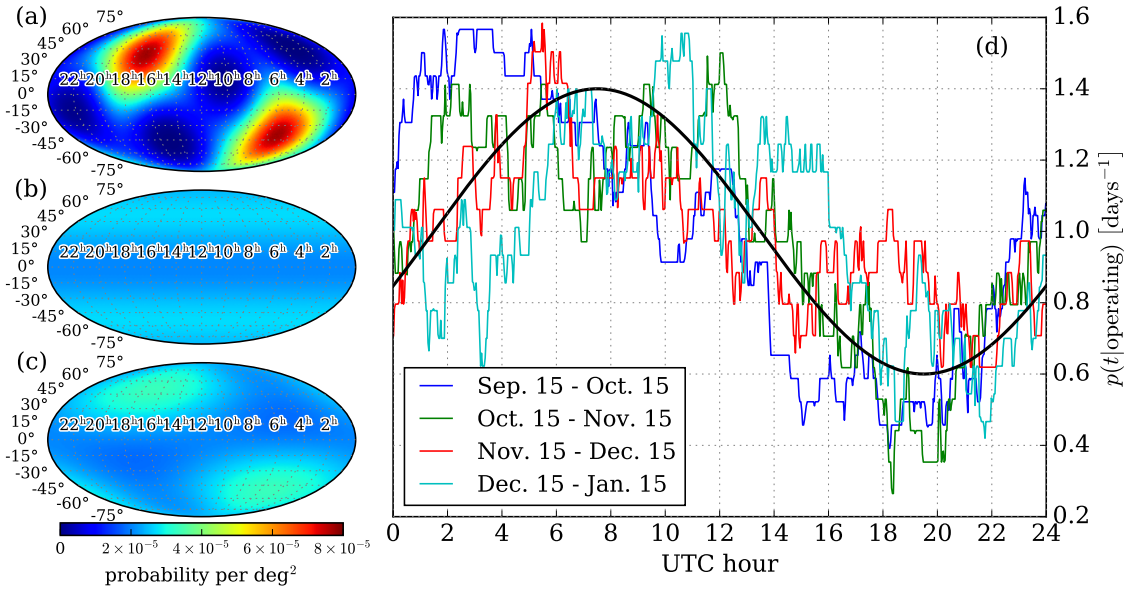

Figure 6.1: (a) The LIGO Hanford and Livingston network antenna pattern in equatorial coordinates at 00:29:18 UTC on Sep. 14, 2015. The maxima lie above North America and the Southern Indian Ocean. (b) The antenna pattern swept over the celestial sphere assuming uniform operation throughout time, resulting in two maxima bands in mid-declinations. (c) The antenna pattern swept over the celestial sphere assuming a typical diurnal cycle. This produces a dependence on right ascension that persists over timescales of a few days to weeks. (d) The observed operation of the LIGO detectors during O1 and a sinusoidal model as a function of UTC time. We require both LIGO detectors to be operating at the same time, although each detector shows similar behavior individually.

6.2.2 Dependence on Right Ascension

The antenna pattern also introduces a dependence on longitude, which translates to a dependence on the right ascension. If the detectors operated uniformly in time, then this right ascension dependence would average away as the Earth rotates. However, because the duty cycle is not uniform in time, this engenders a net bias in favor of certain right ascensions.

Ground-based GW detectors' data acquisition shows a clear diurnal cycle. In previous runs (S6 (Abadie et al., 2012c; Aasi et al., 2013) and earlier) this was due primarily to anthropogenic noise; the detectors observed lower ambient noise at night because humans were less active. During O1, we observed a similar diurnal cycle. Although anthropogenic noise was mitigated by improved seismic isolation, commissioning activities still preferentially occurred during the day at the detector sites. This, combined with a modest duty cycle (Abbott et al., 2016a), generated a non-trivial preference for acquiring data during the sites' night (Fig. 6.1d). We model this preference with a probability distribution for the time of day during which both interferometers are likely to be operating:

$$p(t|\text{operating}) = \frac{1}{\text{day}}\left(1 + A\sin\left(\frac{2\pi t}{\text{day}} - \frac{\pi}{8}\right)\right) \tag{6.1}$$

The amplitude (A) reflects the extent of the day/night bias and is typically near 0.4. This means the detectors are 2.3 times more likely to record data at their local midnight than at noon. We note that this bias may be decreased by reducing the amount of commissioning activity during the day or by increasing the overall duty cycle of the instruments (e.g., reducing the duration of down-time due to events uncorrelated with the diurnal cycle). As the duty cycle increases, the relative importance of the diurnal behavior will decrease (Please see the Appendix for more details.). However, we always expect some small diurnal cycle to be present.

The diurnal cycle preserves the dependence on right ascension as the Earth rotates (Fig

6.1c), which persists over timescales of days to weeks. Figure 6.2 shows the dependence averaged over a month for several months throughout the year. However, over the course of a year, the Earth's orbit will average away this dependence. Nonetheless, as currently scheduled, GW detectors do not operate year-round, instead only recording data over a few consecutive months during observing runs. If observing runs are scheduled during the same season repeatedly, the right ascension dependence introduced by the diurnal cycle can persist for years.

Furthermore, the galactic plane intersects the preferred directions from May through September (Fig. 6.2). Depending on the desired target, this could be an advantage or a hindrance. Detected compact binaries are expected to be extragalactic (Abbott et al., 2016; Abbott et al., 2016b) and the galactic plane will serve as a foreground for any EM follow-up, significantly complicating the removal of transient contaminants. However, detectable core-collapse Supernova are expected to be primarily galactic (Gossan et al., 2016), and therefore GW detectors may have their best chance of observing such events during the North's summer. Regardless of the source, a full understanding of the distribution of detectable signals across both declination and right ascension will be crucial when considering any isotropy or homogeneity measurements using GW observations alone.

6.3 Impact on ground-based electromagnetic follow-up

Selection effects associated with ground-based GW detectors impact EM follow-up facilities. In particular, we focus on three possible effects: the localization probability that a telescope can survey (observable probability), the source's closest angle of approach to an observatory's zenith while the observatory can observe (mimimum zenith distance), and the time until a GW source becomes observable (delay time). We focus on EM follow-up timescales of up to a few days or weeks, and therefore neglect seasonal modulations of the sky over the duration of the EM observations for each individual GW event. This is an appropriate timescale for

short gamma-ray burst optical afterglows (Berger, 2014) and kilonovae (Barnes & Kasen, 2013), two promising EM counterparts of compact binary coalescences involving at least one neutron star. Radio transients may persist over longer timescales and therefore these effects may be less relevant. For these EM follow-up timescales, we consider low-latency GW alerts. In O1, it took a couple of days to issue alerts, but we expect this to be reduced to a few minutes in O2 and beyond (Abbott et al., 2016c). Throughout this chapter, we assume the diurnal cycle modeled in Equation 6.1 as well as 18° of astronomical twilight (Patat et al.,

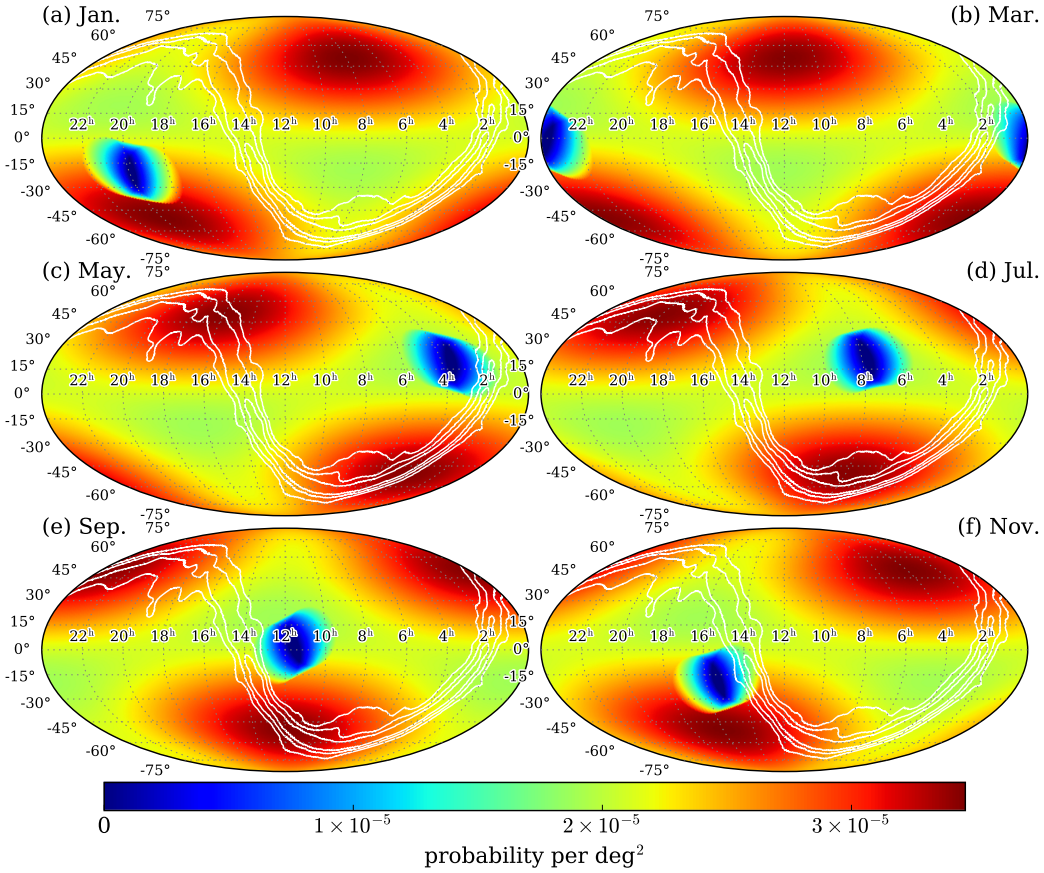

Figure 6.2: The monthly preferred regions for GW detections on the celestial sphere. The Sun occludes a region 18° in radius (assuming observatories can see down to their horizons), and this region is smeared out by averaging over a month. The white contours are the Planck occlusion masks (NASA/IPAC Infrared Science Archive, 2016) and represent the Galactic plane.

2006). We also assume the observatories can observe within 90° of their zenith.

In the limit of a large number of detections, the combined posterior distributions trace out the network antenna pattern. In what follows, we use the antenna pattern to approximate limiting distribution of many events (Please see the Appendix for more details.). To quantify departures from this limit when only a few events are available, we simulate collections of events based on binary black hole localizations with two detectors (Essick et al., 2015). We find good agreement.

6.3.1 Observable Probability

GW localizations are driven by triangulation and, for networks of two detectors, the localization is characterized by large rings that can span hundreds of square degrees regardless of source morphology. Furthermore, these error regions typically have support at antipodal points on the sky, making it difficult for a single EM observatory to access the entire skymap. This is compounded by solar occlusion, which renders certain parts of the sky inaccessible. We ignore lunar occlusion because, unlike solar occlusion, it is not thought to systematically correlate with when the detectors operate. Because we focus on timescales of a few days, we assume the Earth will revolve at least once. Therefore, the observable region depends only on the observatory's latitude.

Figure 6.3 shows the observable probability as a function of latitude for a year-long average and for the solstices. We define

$$p_{\rm obs}(\mathrm{lat}_{\rm site}) = \int dt \left(p(t|\mathrm{operating}) \int d\Omega \, p_{GW}(\Omega, t) \Theta_{\rm obs}(\Omega, t, \mathrm{lat}_{\rm site}) \right) \tag{6.2}$$

where $p_{GW}(\Omega, t)$ is the probability density of the GW source coming from Ω (at time t), and $\Theta_{\rm obs}$ is the region accessible from a particular latitude at t, respectively. We see sharp declines near latitudes of $\pm 50^\circ$ corresponding to the Arctic/Antarctic circles and astronomical

twilight, but otherwise $p_{\rm obs}$ follows a smooth distribution favoring equatorial observatories. This is because equatorial observatories can systematically access sources in both hemispheres, whereas other observatories may be confined to only the probability within their own. While equatorial facilities are favored overall, mid-latitudes have larger $p_{\rm obs}$ than they would for isotropically distributed detections. This will persist regardless of the day/night cycle and is driven solely by the GW detectors' latitudes. We note that the optimal observing months of the Northern and Southern hemispheres are out of phase (Fig. 6.3). For example, if LIGO operates from September to February, the Northern hemisphere will have a better chance of observing counterparts than the Southern hemisphere.

While $p_{\rm obs}$ does not depend on the longitude, the diurnal cycle can still introduce a systematic bias. This is because the Sun will be systematically out of phase with the Northern maximum of the antenna pattern (Fig. 6.2). We find that this typically produces an increase in $p_{\rm obs}$ of a few percent for mid-latitudes in the North, even though their analogs in the South have larger $p_{\rm obs}$ because of the shorter solar exposure over an entire year.

We note that $p_{\rm obs}$ reflects the amount of localization probability that is observable in the limit of many detections. Outside of this limit, we consider an analogous quantity ($\hat{p}_{\rm obs}$) defined for a finite number of detections (N_d) with the correspondence $p_{\rm obs} = \lim_{N_d\to\infty} \hat{p}_{\rm obs}$ (Please see the Appendix for more details.). Statistical fluctuations in $\hat{p}_{\rm obs}$, caused by variations in which events occur, can be large, particularly with $\lesssim$10 events. We expect the uncertainty in this estimate to scale inversely with $\sqrt{N_d}$, and Figure 6.3 reports $\lim_{N_d\to\infty}(N_d/10)^{1/2}\sigma_{\hat{p}_{\rm obs}}$ as error bars along with the mean. Typical values are between 6–10%. We also note that the intrinsic distribution for single events ($N_d = 1$) may not be Gaussian but, in the limit of many detections, the distribution of the mean will be.

6.3.2 Minimum Zenith Distance

While equatorial observatories may be able to access the largest integrated probability, and thereby have the largest probability of being able to image a source, this does not necessarily imply that they will have the best conditions for observing. An important consideration is the closest approach of each field to an observatory's zenith (minimum zenith distance). Sources at large angles from an observatory's zenith can be difficult to observe because of high airmass and mechanical limitations. In Fig. 6.4 we present the mean minimum zenith distance, as a function of latitude, weighted by the probability that the source actually comes from each location:

$$D_{\rm zen}(\mathrm{lat_{site}}) = \frac{1}{p_{\rm obs}} \int dt \left(p(t|\mathrm{operating}) \int d\Omega \, p_{GW}(\Omega, t) \Theta_{\rm obs}(\Omega, t, \mathrm{lat_{site}}) D_{\rm zen}(\Omega, t, \mathrm{lat_{site}}) \right) \tag{6.3}$$

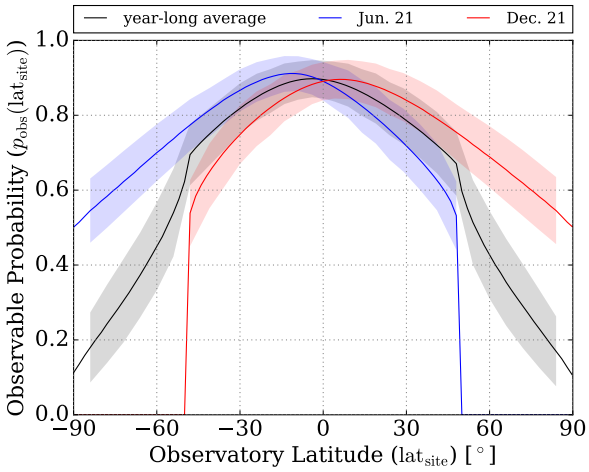

Figure 6.3: $p_{\rm obs}(\mathrm{lat_{site}})$ averaged over a year (black), near the Northern summer solstice (blue), and near the Northern winter solstice (red). Shaded regions correspond to the fluctuations from localization maps simulations ($\lim_{N_d \to \infty} (N_d/10)^{1/2} \sigma_{\hat{p}_{\rm obs}}$).

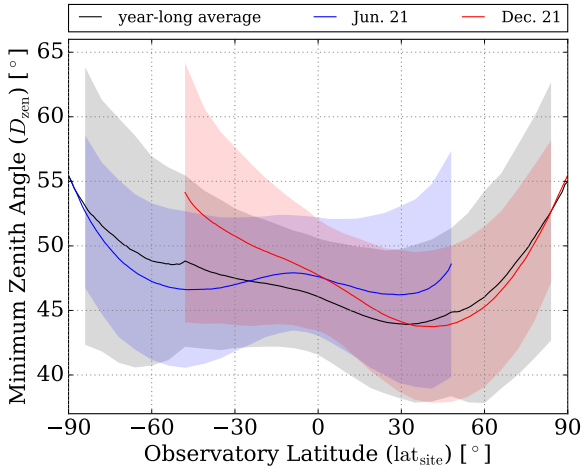

Figure 6.4: $D_{\rm zen}$ averaged over a year (black), near the Northern summer solstice (blue), and near the Northern winter soltice (red). Shaded regions correspond to the fluctuations from localization maps simulations ($\lim_{N_d \to \infty} (N_d/10)^{1/2} \sigma_{\hat{D}_{\rm zen}}$), and we note that $\hat{D}_{\rm zen}$'s distribution is quite broad.

$\Theta_{\rm obs}$ accounts for solar occlusion and $D_{\rm zen}(\Omega, t, {\rm lat}_{\rm site})$ incorporates when the EM facility will actually be able to observe. We find that observatories at extreme latitudes ($\pm 90^\circ$) will almost always have large $D_{\rm zen}$, with a gradual transition to lower values at lower latitudes. There is a $\sim 10\%$ difference in $D_{\rm zen}$ between observatories at mid-latitudes, with Northern sites preferred. This is because the diurnal cycle makes the Sun preferentially overlap the Southern antenna pattern and forces Southern facilities to observe closer to sunrise and sunset than their Northern counterparts. This behavior is particularly evident at the Northern winter solstice.

Fig. 6.4 also shows the fluctuations in the analgous stastic defined for a finite number of detections ($\hat{D}_{\rm zen}$). We typically find $\lim_{N_d \to \infty} (N_d/10)^{1/2} \sigma_{\hat{D}_{\rm zen}} \sim 4$–$10^\circ$ (Please see the Appendix for more details.). Furthemore, $D_{\rm zen}$ corresponds to the mean of many events. For a single event, the mode of $\hat{D}_{\rm zen}(N_d = 1)$'s distribution falls near 20° at mid-latitudes in the North and 60° in the South, whereas the mode is near 50° at both poles.

6.3.3 Delay Time

For counterparts with timescales of days, EM observatories' longitudes can play an important role. This is because observatories will have to wait to begin observing until the source rises at their location. This can be exacerbated by the position of the Sun, which will systematically correlate with the diurnal cycle.

We expect that the amount of time an observatory must wait before commencing observations (delay time) will depend on both the observatory's longitude and latitude and define

$$D_{\rm del}(\Omega_{\rm site}) = \frac{1}{p_{\rm obs}} \int dt \left(p(t|{\rm operating}) \int d\Omega \, p_{GW}(\Omega, t) \Theta_{\rm obs}(\Omega, t, {\rm lat}_{\rm site}) D_{\rm del}(\Omega, t, \Omega_{\rm site}) \right) \tag{6.4}$$

where $D_{\rm del}(\Omega_{\rm site}, t, \Omega)$ accounts for sunrise and sunset along with the source's relative po-

sition to the observatory. We restrict ourselves to only the parts of the skymap that are actually accessible from each site. Fig. 6.5 shows the dependence on the observatory's longitude and latitude. Although the shape changes, we see a reasonably uniform distribution of $D_{\rm del}$ throughout the globe (there are slightly longer delay times in the North compared to their analogs in the South away from the blob over Africa) with the notable exception of the Southern Atlantic, Africa, and the Indian Ocean, particularly in the year-long average (Fig 6.5e). Because the majority of detections will occur during North America's night, these locations are likely to already be in daylight and will therefore have to wait for sunset. Furthermore, observatories in the South will have to wait until their zenith is very close to the source's right ascension before they observe, which explains why the blob is wider in the South. From simulations outside the limit of many detections, we also note that the distribution of the analogous statistic ($\hat{D}_{\rm del}(N_d = 1)$) is very non-Gaussian and very skew right. However, the mean is still Gaussian as $N_d \to \infty$ with an associated variance $\lim_{N_d\to\infty}(N_d/10)^{1/2}\sigma_{\hat{D}_{\rm del}} \sim$ 80–240 minutes, with most values near 100 minutes, depending on the observatory's location (Please see the Appendix for more details.).

We note that if the diurnal cycle were to be strongly reduced or eliminated, the blob above Africa would become less prominent and an analogous blob would appear in the Northern Pacific. The latter corresponds to observatories that are in daylight when a source is detected above the Southern antenna pattern. The overall effect of removing the diurnal cycle, however, is toward a more uniform distribution of delay times across the entire globe.

6.4 Discussion

In this chapter, we enumerate three effects that imprint selection effects on the distribution of GW detections, which will be relevant for all types of GW sources: (i) the detectors locations introduce a preference for mid-declinations, (ii) a diurnal cycle modulates when the detectors operate and produces a sky sensitivity with a dependence on the right ascension

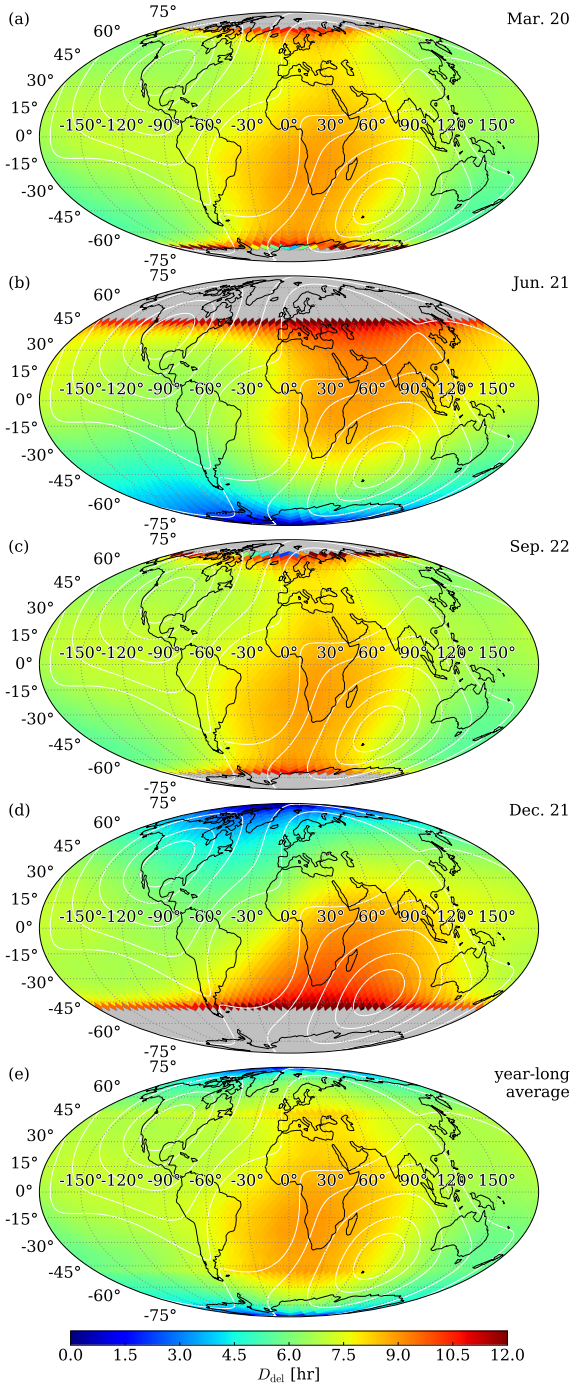

Figure 6.5: $D_{\mathrm{del}}(\Omega_{\mathrm{site}})$ for hypothetical observatories placed throughout the globe for times surrounding the Northern (a) spring equinox, (b) summer solstice, (c) fall equinox, and (d) winter solstice. (e) Shows a year-long average. Grey regions correspond to observatories that are in perpetual daylight or twilight at the corresponding time.

over short time-scales, and, (iii) if detections are made only during relatively short observing runs, the right ascension bias can be imprinted over longer timescales. While the effects are important when modeling the expected distribution of GW detections on the sky, they can also have significant implications for EM follow-up.

In general, ground-based EM observatories located at latitudes comparable to those of the GW detectors are preferred. While equatorial sites can access the largest fraction of the sky, mid-latitude sites in the North will be able to observe more events closer to their zenith without sacrificing much coverage. Furthermore, there is a preference for EM observatories located near the same longitude as the GW detectors, or slightly West thereof, assuming the EM facilities can begin observing quickly and that counterparts decay with timescales of hours. This leads us to the conclusion that EM facilities located near the GW detectors are favored by how the GW detectors' actually operate.

In addition to informing follow-up efforts for GW candidates, our results may help guide EM activities *in advance* of GW observations. For example, because we know which parts of the celestial sphere are most likely to host detectable GW events, we can build up relevant templates for image subtraction before GW observations even begin, focusing particularly on the highest probability regions. Galaxy catalog constructions could be focused similarly. In addition, surveys may focus their observations near the peak of the instantaneous antenna pattern, thereby anticipating where detectable GW sources are most likely to occur and facilitating target of opportunity follow-ups. This will also increase the probability of serendipitous detection of prompt EM counterparts. We note that EM observatories located near GW detectors will naturally survey a maximum of the antenna pattern because their zenith lies near that maximum automatically.

The behavior of GW observatories can become more complicated as the global network of detectors expands. A larger network increases the uniformity of sensitivity to GW signals across the sky, and therefore reduces the selection effects in both declination and right ascen-

sion. Furthermore, detectors located around the globe will likely experience diurnal cycles that are out of phase, further reducing any preference for certain right ascensions. However, because all planned detectors lie within a relatively confined band of latitudes (Acernese et al., 2015; Aso et al., 2013; Fairhurst, 2014), the bias on declination may persist at some level. In addition, the LIGO detectors will likely have the best sensitivity in the network for at least the next few years (Abbott et al., 2016a). This means that they will generally provide the dominant contribution to detections, and the observed distribution of sources will follow their antenna pattern. Thus, our analysis serves as a reasonable prediction for both the distributions of GW detections as well as their impact on EM follow-up efforts for the next few years.

We want to thank Lisa Barsotti, Matt Evans, and Rich Middleman for discussions about locking behavior, commissioning, and anthropogenic noise sources, James Annis for discussions about EM observations, and Marica Branchesi for very helpful comments.

REFERENCES

Aasi, J., Abadie, J., Abbott, B. P., et al. 2013, Phys. Rev. D, 88, 062001

Aasi, J., Abadie, J., Abbott, B. P., et al. 2013, Phys. Rev. D, 87, 022002

Aasi, J., Abadie, J., Abbott, B. P., et al. 2014, Astrophys. J. Suppl. Ser., 211, 7

Aasi, J., Abadie, J., Abbott, B. P., et al. 2015, Classical and Quantum Gravity, 32, 115012

Abadie, J., et al. 2010a, Class. Quantum Grav., 27, 173001

—. 2010b, Phys. Rev. D, 82, 102001

Abadie, J., Abbott, B. P., Abbott, R., et al. 2010, Classical and Quantum Gravity, 27, 173001

—. 2012a, Astron. Astrophys., 541, A155

—. 2012b, Astrophys. J., 760, 12

—. 2012c, Phys. Rev. D, 85, 082002

Abadie, J., et al. 2012, arXiv:1203.2674

Abbott, B. P., Abbott, R., Abbott, T. D., et al. 2016a, Astrophys. J. Lett., 818, L22

—. 2016b, Physical Review X, 6, 041015

Abbott, B. P., Abbott, R., Abbott, T. D., et al. 2016, Classical and Quantum Gravity, 33, 134001

Abbott, B. P., Abbott, R., Abbott, T. D., et al. 2016a, Physical Review Letters, 116, 131103

—. 2016b, Physical Review Letters, 116, 241103

—. 2016c, Astrophys. J. Lett., 826, L13

Abbott, B. P., Abbott, R., Abbott, T. D., et al. 2016, Phys. Rev. Lett., 116, 061102

Abbott, B. P., Abbott, R., Abbott, T. D., et al. 2016a, Living Reviews in Relativity, 19, arXiv:1304.0670

—. 2016b, Physical Review Letters, 116, 221101

—. 2016c, Astrophys. J. Lett., 833, L1

—. 2016d, Astrophys. J. Lett., 832, L21

—. 2017a, Physical Review Letters, 119, 161101

—. 2017b, Astrophys. J. Lett., 848, L12

Acernese, F., Agathos, M., Agatsuma, K., et al. 2015, Classical and Quantum Gravity, 32, 024001

Acernese, F., Agathos, M., Agatsuma, K., et al. 2015, Classical and Quantum Gravity, 32, 024001

Annis, J., Soares-Santos, M., Berger, E., et al. 2016, Astrophys. J. Lett., 823, L34

Aso, Y., Michimura, Y., Somiya, K., et al. 2013, Phys. Rev. D, 88, 043007

Bailyn, C. D., Jain, R. K., Coppi, P., & Orosz, J. A. 1998, Astrophys. J., 499, 367

Barnes, J., & Kasen, D. 2013, Astrophys. J., 775, 18

Bauswein, A., & Janka, H.-T. 2012, Physical Review Letters, 108, 011101

Belczynski, K., Dominik, M., Bulik, T., et al. 2010, Astrophys. J. Lett., 715, L138

Belczynski, K., Holz, D. E., Bulik, T., & O'Shaughnessy, R. 2016a, Nature, 534, 512

Belczynski, K., Perna, R., Bulik, T., et al. 2006, Astrophys. J., 648, 1110

Belczynski, K., Repetto, S., Holz, D. E., et al. 2016b, Astrophys. J., 819, 108

Belczynski, K., Wiktorowicz, G., Fryer, C. L., Holz, D. E., & Kalogera, V. 2012, Astrophys. J., 757, 91

Berger, E. 2011, New. Astron. Rev., 55, 1

—. 2014, Annu. Rev. Aston. Astrophys., 52, 43

Berger, E., Fong, W., & Chornock, R. 2013, Astrophys. J. Lett., 774, L23

Berger, E., Fox, D. B., Price, P. A., et al. 2007, Astrophys. J., 664, 1000

Berry, C. P. L., Mandel, I., Middleton, H., et al. 2015, Astrophys. J., 804, 114

Biswas, R., Brady, P. R., Creighton, J. D. E., & Fairhurst, S. 2009, Classical and Quantum Gravity, 26, 175009

Bloom, J. S., Holz, D. E., Hughes, S. A., et al. 2009, arXiv:0902.1527

Briggs, M. S., Connaughton, V., Meegan, C. A., et al. 2009, in American Institute of Physics Conference Series, Vol. 1133, American Institute of Physics Conference Series, ed. C. Meegan, C. Kouveliotou, & N. Gehrels, 40–42

Burrows, D. N., Grupe, D., Capalbi, M., et al. 2006, Astrophys. J., 653, 468

Cannon, K., Cariou, R., Chapman, A., et al. 2012, Astrophys. J., 748, 136

Chen, H.-Y., & Holz, D. E. 2013, Physical Review Letters, 111, 181101

—. 2014, ArXiv e-prints, arXiv:1409.0522

—. 2015, ArXiv e-prints, arXiv:1509.00055

—. 2016, ArXiv e-prints, arXiv:1612.01471

Chu, Q., Howell, E. J., Rowlinson, A., et al. 2016, Mon. Not. R. Astron. Soc., 459, 121

Church, R. P., Levan, A. J., Davies, M. B., & Tanvir, N. 2011, Mon. Not. R. Astron. Soc., 413, 2004

Coward, D., Howell, E., Piran, T., et al. 2012, arXiv:1202.2179

Cowperthwaite, P. S., Berger, E., Soares-Santos, M., et al. 2016, Astrophys. J. Lett., 826, L29

Cutler, C., & Flanagan, É. E. 1994, Phys. Rev. D, 49, 2658

Dalal, N., Holz, D. E., Hughes, S. A., & Jain, B. 2006, Phys. Rev. D, 74, 063006

Del Pozzo, W. 2012, Phys. Rev. D, 86, 043011

—. 2014, Journal of Physics Conference Series, 484, 012030

Dietz, A. 2011, Astron. Astrophys., 529, A97

Dominik, M., Belczynski, K., Fryer, C., et al. 2012, arXiv:1202.4901

Einstein, A. 1916, Sitzungsberichte der Königlich Preußischen Akademie der Wissenschaften (Berlin), 688

—. 1918, Sitzungsberichte der Königlich Preußischen Akademie der Wissenschaften (Berlin), Seite 154-167.

Essick, R., Vitale, S., Katsavounidis, E., Vedovato, G., & Klimenko, S. 2015, The Astrophysical Journal, 800, 81

Evans, P. A., Fridriksson, J. K., Gehrels, N., et al. 2012, Astrophys. J. Suppl. Ser., 203, 28

Fairhurst, S. 2009, New Journal of Physics, 11, 123006

—. 2011, Classical and Quantum Gravity, 28, 105021

Fairhurst, S. 2014, Journal of Physics: Conference Series, 484, 012007

Farr, B., Berry, C. P. L., Farr, W. M., et al. 2016, Astrophys. J., 825, 116

Fong, W., & Berger, E. 2013, Astrophys. J., 776, 18

Fong, W., Berger, E., & Fox, D. B. 2010, Astrophys. J., 708, 9

Fong, W., Berger, E., Margutti, R., et al. 2012, Astrophys. J., 756, 189

Fong, W., Berger, E., Chornock, R., et al. 2013, Astrophys. J., 769, 56

Freiburghaus, C., Rosswog, S., & Thielemann, F.-K. 1999, Astrophys. J. Lett., 525, L121

Gehrels, N., Cannizzo, J. K., Kanner, J., et al. 2016, Astrophys. J., 820, 136

González, R. E., Lares, M., Lambas, D. G., & Valotto, C. 2006, Astron. Astrophys., 445, 51

Gossan, S. E., Sutton, P., Stuver, A., et al. 2016, Phys. Rev. D, 93, 042002

Grover, K., Fairhurst, S., Farr, B. F., et al. 2014, Phys. Rev. D, 89, 042004

Hanna, C., Mandel, I., & Vousden, W. 2014, Astrophys. J., 784, 8

Hebeler, K., Lattimer, J. M., Pethick, C. J., & Schwenk, A. 2013, Astrophys. J., 773, 11

Hild, S., Chelkowski, S., & Freise, A. 2008, ArXiv e-prints, arXiv:0810.0604

Holz, D. E., & Hughes, S. A. 2005, Astrophys. J., 629, 15

Holz, D. E., & Linder, E. V. 2005, Astrophys. J., 631, 678

Hughes, S. A., & Menou, K. 2005, Astrophys. J., 623, 689

Hulse, R. A., & Taylor, J. H. 1975, Astrophys. J. Lett., 195, L51

Janka, H.-T., Mazzali, P., Aloy, M.-A., & Pian, E. 2006, Astrophys. J., 645, 1305

Kasliwal, M. M., & Nissanke, S. 2014, The Astrophysical Journal Letters, 789, L5

Khan, S., Husa, S., Hannam, M., et al. 2016, Phys. Rev. D, 93, 044007

Kocevski, D., Thöne, C. C., Ramirez-Ruiz, E., et al. 2010, Mon. Not. R. Astron. Soc., 404, 963

Liske, J., Lemon, D. J., Driver, S. P., Cross, N. J. G., & Couch, W. J. 2003, Mon. Not. R. Astron. Soc., 344, 307

Littenberg, T. B., Farr, B., Coughlin, S., Kalogera, V., & Holz, D. E. 2015, Astrophys. J. Lett., 807, L24

Metzger, B. D., & Berger, E. 2012, Astrophys. J., 746, 48

Metzger, B. D., Martínez-Pinedo, G., Darbha, S., et al. 2010, Mon. Not. R. Astron. Soc., 406, 2650

Nakar, E., Gal-Yam, A., & Fox, D. B. 2006, Astrophys. J., 650, 281

NASA/IPAC Infrared Science Archive. 2016, Planck Public Data Release 2 Mission Ancillary Data, ,

Nissanke, S., Holz, D. E., Dalal, N., et al. 2013a, arXiv:1307.2638, arXiv:1307.2638

Nissanke, S., Holz, D. E., Hughes, S. A., Dalal, N., & Sievers, J. L. 2010, Astrophys. J., 725, 496

Nissanke, S., Kasliwal, M., & Georgieva, A. 2013b, Astrophys. J., 767, 124

Nissanke, S., Sievers, J., Dalal, N., & Holz, D. 2011, Astrophys. J., 739, 99

Nitz, A. H., Lundgren, A., Brown, D. A., et al. 2013, Phys. Rev. D, 88, 124039

Norberg, P., Cole, S., Baugh, C. M., et al. 2002, Mon. Not. R. Astron. Soc., 336, 907

O'Shaughnessy, R., Kim, C., Kalogera, V., & Belczynski, K. 2008, Astrophys. J., 672, 479

Panaitescu, A. 2006, Mon. Not. R. Astron. Soc.: Letters, 367, L42

Patat, F., Ugolnikov, O. S., & Postylyakov, O. V. 2006, Astron. Astrophys., 455, 385

Perley, D. A., Metzger, B. D., Granot, J., et al. 2009, Astrophys. J., 696, 1871

Planck Collaboration, Ade, P. A. R., Aghanim, N., et al. 2016, Astron. Astrophys., 594, A13

Popham, R., Woosley, S., & Fryer, C. 1999, Astrophys. J., 518, 356

Press, W. H., Teukolsky, S. A., Vetterling, W. T., & Flannery, B. P. 2007, Numerical Recipes 3rd Edition: The Art of Scientific Computing, 3rd edn. (New York, NY, USA: Cambridge University Press)

Rezzolla, L., Giacomazzo, B., Baiotti, L., et al. 2011, Astrophys. J., 732, L6

Rosswog, S., & Ramirez-Ruiz, E. 2002, Astrophys. J., 336, L7

Sathyaprakash, B. S., & Schutz, B. F. 2009, Living Reviews in Relativity, 12, 2

Schechter, P. 1976, Astrophys. J., 203, 297

Schmidt, M. 1968, Astrophys. J., 151, 393

Schutz, B. F. 1986, Nature, 323, 310

—. 2011, Classical and Quantum Gravity, 28, 125023

Singer, L. P., & Price, L. R. 2016, Phys. Rev. D, 93, 024013

Singer, L. P., Price, L. R., Farr, B., et al. 2014, The Astrophysical Journal, 795, 105

Singer, L. P., Chen, H.-Y., Holz, D. E., et al. 2016a, Astrophys. J. Lett., 829, L15

—. 2016b, Astrophys. J.s, 226, 10

Soares-Santos, M., Kessler, R., Berger, E., et al. 2016, Astrophys. J. Lett., 823, L33

Soderberg, A. M., Berger, E., Kasliwal, M., et al. 2006, Astrophys. J., 650, 261

Takami, K., Rezzolla, L., & Baiotti, L. 2014, Physical Review Letters, 113, 091104

Tanvir, N. R., Levan, A. J., Fruchter, A. S., et al. 2013, Nature, 500, 547

Taylor, J. H., & Weisberg, J. M. 1982, Astrophys. J., 253, 908

Thorne, K. S. 1987a, Gravitational radiation. (Cambridge University Press, Cambridge, England), 330–458

—. 1987b, Gravitational radiation., ed. S. W. Hawking & W. Israel, 330–458

Vallisneri, M. 2012, Phys. Rev. D, 86, 082001

Veitch, J., Raymond, V., Farr, B., et al. 2015, Phys. Rev. D, 91, 042003

Wen, L., & Chen, Y. 2010, Phys. Rev. D, 81, 082001

Yunes, N., Arun, K. G., Berti, E., & Will, C. M. 2009, Phys. Rev. D, 80, 084001

Yunes, N., Yagi, K., & Pretorius, F. 2016, Phys. Rev. D, 94, 084002